Tribology International 165 (2022) 107317

Contents lists available at ScienceDirect

Tribology International

journal homepage: www.elsevier.com/locate/triboint

A computationally efficient method for the prediction of fretting wear in practical engineering applications

Y. Kong, C.J. Bennett [*], C.J. Hyde

Gas Turbine and Transmissions Research Centre, Faculty of Engineering, The University of Nottingham, Nottingham NG7 2RD, UK

ARTICLE INFO

Keywords:
fretting
fretting wear
numerical wear modeling
wear simulation

ABSTRACT

A method for simulating fretting wear using the Modified Simplex Method for a contact solution has been developed. The initial separation between two contacting bodies was used as an input to solve the contact force distribution. An average cycle pressure distribution was calculated for the stationary surface over a displacement cycle. The wear depth was calculated for each body based on the modified Archard's wear equation using the force distributions and the gross sliding distance. The initial separation was updated and the force distribution was solved for the next iteration. Methods for optimizing computational time are presented using a combination of linear jumping and adaptive cycle jumping for the wear depths, and an interpolation weighting method for reducing the grid size. It was found that computational time can be reduced by at least 98% compared with other simulation methods, making this method a viable tool for design. Fretting wear scars and depths were simulated for a cylinder on flat in contact and were found to agree with experimental results and Finite Element modeling results from previous literature. To show the capability of the fretting wear model, three practical applications were simulated: automotive seat sliding rails, steel wire ropes for industrial applications and steam generator tubes for nuclear power stations.

1. Introduction

Fretting wear occurs due to small oscillatory relative movement between contacting surfaces under a normal load. The main modes of fretting wear are split into tangential, radial, torsional and rotational modes [1] with the most commonly investigated being tangential fretting wear. There are two running statuses of fretting wear: gross-slip, where slip occurs across the whole region of contact; and partial slip, where there is no relative movement, or 'stick' in parts of the region of contact. Fretting wear generally dominates as the main damage mechanism over fretting fatigue under gross-slip conditions. Fretting wear can cause significant damage, reducing the life and integrity of components; example applications where fretting wear is an issue include spline couplings [2,3], industrial steel ropes [4], steam turbine blades [5], steam generator tubing for nuclear power plants [6–10], electrical connectors [11,12] and sliding seat rails for automotive applications [13]. There are several factors that influence fretting wear behavior [14], which includes contact geometry, normal loading, sliding amplitude and frequency; many authors have investigated the influence of these by a series of fretting tests [15–17]. For life prediction and design optimization of components, fretting experiments are not always ideal. These are very involved, require many tests and a high number of cycles, and are therefore time consuming. Numerical modeling is vital to the understanding of fretting wear, as a collection of test cases can be predicted and compared, and the evolution of fretting wear can be investigated.

A popular method to model fretting wear involves calculating local contact pressures and slips using a contact solver and evaluating the incremental wear depth using a wear law. The contact geometry is readjusted based on the material removed due to wear and this is iteratively calculated until the total number of cycles is reached. This takes into account the nonlinearity of wear due to the geometry changes. This approach was initially developed by McColl et al. [18], who used Finite Element Analysis (FEA) as the contact solver, which has commonly been used for fretting wear problem as it is versatile in modeling any geometry and additional loading [18–29]. This approach, however, is computationally expensive, especially for refined meshes, 3D geometries and high number of cycles typically required for the prediction of fretting wear, making its use impractical for iterative or generative design processes for applications involving this phenomenon. It is

---

[*] Corresponding author.
E-mail address: C.Bennett@nottingham.ac.uk (C.J. Bennett).

https://doi.org/10.1016/j.triboint.2021.107317
Received 16 July 2021; Received in revised form 13 October 2021; Accepted 14 October 2021

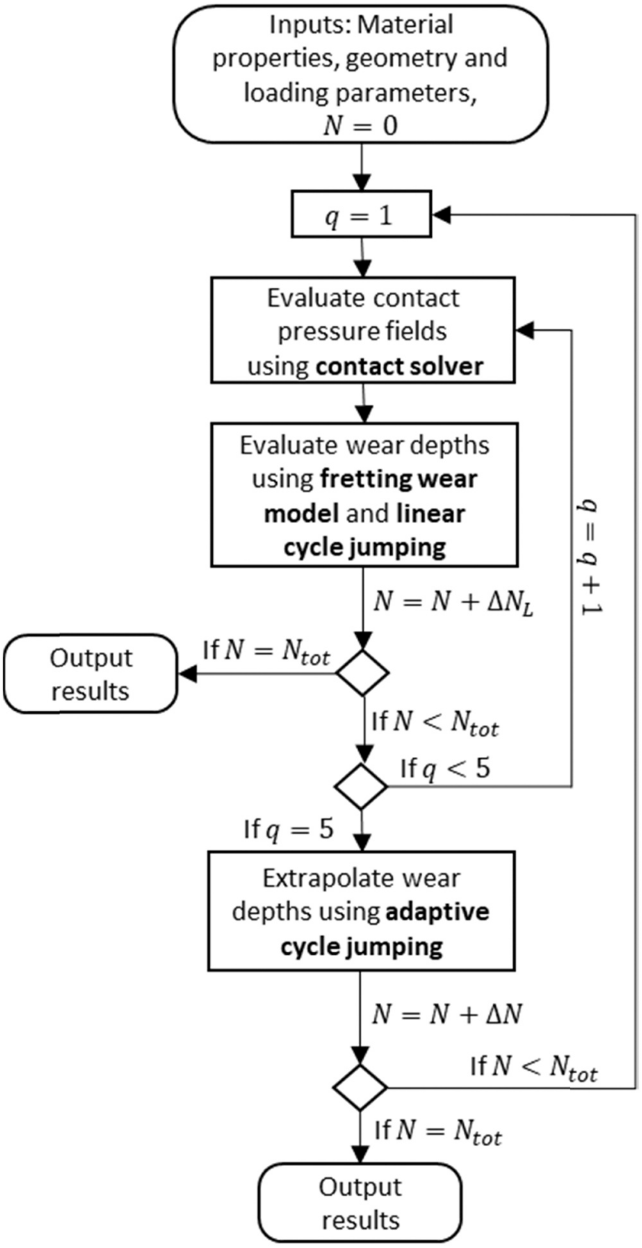

Fig. 1. Summarized flowchart of the modeling methodology (where N is the current cycle number, ΔN_L is the linear cycle jump and ΔN is the adaptive cycle jump).

especially impractical for industrial applications where the number of cycles are typically higher than 1 million cycles [2,5], which has not yet been modeled in previous literature. Therefore, alternative numerical methods used for modeling contact include the boundary element method (BEM) and mathematical programming methods (MPMs). The advantage of these methods are that they discretize the contact surfaces instead of the whole body, thereby reducing the total number of degrees of freedom required compared with FEA and, therefore, reducing simulation time and increasing calculation efficiency. BEM involves the matrix inversion technique and an iterative process to solve for the boundary integral equations required for contact, whereas MPMs solve the equations required for contact by treating the contact problem as a mathematical program and using an optimization or iterative algorithm. The BEM has successfully been used for 2D and 3D fretting wear simulations [30,31] and has proven to improve simulation time in comparison with FEA based simulations [30]. MPMs that are commonly used as contact solvers include quadratic programming [32], conjugate gradient method (CGM) [33–38] and the Modified Simplex Method (MSM) for linear programming [39–46]. Quadratic programming has been used for 2D fretting wear simulations [32] and CGM has been used for 3D fretting wear simulations [33–37]. For BEM or MPMs, influence coefficients for elastic behavior can be solved either by FEA [38,45,46] or by using an analytical solution. Analytical solutions allow more refined meshes to be solved for a reduced amount of computational time with the help of acceleration techniques. Generally, the analytical solution uses a method by Boussinesq and Cerruti [47] to solve for the elastic displacements due to the contact forces by treating the contacting surfaces as elastic half-spaces [30,33–37]. This can be expanded to include other influence coefficients for more complex geometries and loadings, such as using the MSM for spline couplings which included the effects of torsion, shear, bending and foundation deflections [43,44].

Current fretting wear modeling methods are generally limited to simplified laboratory geometries and published works shows that models have not been applied beyond ~100,000 cycles [31,35,38]. Therefore, the aim of this study is to develop a fretting wear model that can be used for design optimization for a high number of cycles, and for practical geometries and loading. A fretting wear model has been developed using the MSM with the modified Archard's wear equation, whereby fretting wear scars and fretting wear depths are benchmarked and validated against FEA and experimental results from previous literature for cylinder on flat geometry. A finite space model was used for the contact compliance for the elastic deformation to be more representative for the geometry used in experiments. To reduce simulation time of the contact solver, an interpolation method is presented to accelerate simulation time for a refined grid. A technique to reduce calculation time for the total wear depth has been introduced by combining the linear cycle jump technique with an adaptive cycling jump method using the 2nd order Taylor series expansion. The computational time from the developed methods are compared with FEA and BEM methods. Combining the developed methods has allowed 1 million cycles to be modeled, and wear profiles have been validated with previous experimental results. The fretting wear model was also applied to three practical applications for alternative geometries, loading and materials to show the versatility of the model.

2. Modeling methodology

A fretting wear model was developed and implemented in MATLAB 2018b as summarized in Fig. 1. This model consisted of a contact solver for calculating local contact pressures and a fretting wear model which determines the resulting wear depths. Linear and adaptive cycle jumping were also included to reduce the computational time.

2.1. Contact solver

The contact solver was based on a mathematical programming method, known as the Modified Simplex Method (MSM) [39,41], which was developed for general 3D elastic bodies in contact with an applied normal load. It is an optimization algorithm, which solves for linear constraints with a criterion for contact to obtain the load distribution across the contacting surfaces. The method assumed that the contact is frictionless, the deformations are small, both bodies are linear elastic and the surfaces are smooth. The proposed contact zone was a 2D contact surface, which was discretised into rectangular elements in a rectangular grid by M_x columns by M_y rows. The contact forces were solved at the center of each element, i. An example of a cylinder on flat set up with a proposed contact zone and discretization shown is shown in Fig. 2.

At any element, i, the final separation, Y_i, between both contacting bodies at this point was equal to the sum of the initial separation, ε_i, and the normal elastic deformations of both bodies, δ_i^1 and δ_i^2 (moving body and stationary body, respectively), minus the rigid body approach, α:

$$Y_i = \varepsilon_i + \delta_i^1 + \delta_i^2 - \alpha \tag{1}$$

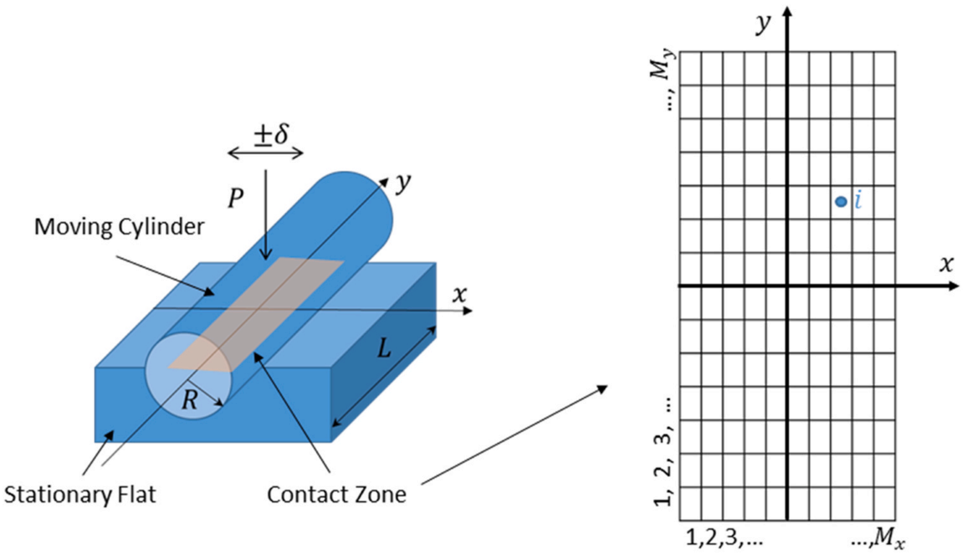

Fig. 2. Schematic of geometry and loading for a cylinder on flat with the discretised contact zone.

where $Y_i \geq 0$ due to elasticity.

When the final separation of an arbitrary contact pair is equal to 0 (and therefore, in contact), then there must be a contact force and if the final separation is greater than 0, then there is no contact force. Therefore, for all contact pairs, the criterion of contact was given by:

$$\left\{\begin{matrix} Y_i > 0, & F_i = 0, \\ Y_i = 0, & F_i > 0, \end{matrix} \quad i \in [1, n]\right\} \tag{2}$$

where F_i is the contact force and n is the total number of contact pairs. The condition of equilibrium was given by:

$$\sum_{i=1}^{n} F_i = P \tag{3}$$

where the sum of all the contact forces at each contact pair must equal the total applied load, P.

The normal elastic deformations of both bodies are defined by the total compliance matrix, $\boldsymbol{C}$, multiplied by the contact force vector, $\boldsymbol{F}$, given by the following:

$$\boldsymbol{\delta}^1 + \boldsymbol{\delta}^2 = \boldsymbol{CF} \tag{4}$$

$$\boldsymbol{C} = \boldsymbol{C}^1 + \boldsymbol{C}^2 = \begin{bmatrix} c_{11} & c_{12} & \cdots & c_{1n} \\ c_{21} & c_{22} & \cdots & c_{2n} \\ \vdots & \vdots & \ddots & \vdots \\ c_{n1} & c_{n2} & \cdots & c_{nn} \end{bmatrix}^1 + \begin{bmatrix} c_{11} & c_{12} & \cdots & c_{1n} \\ c_{21} & c_{22} & \cdots & c_{2n} \\ \vdots & \vdots & \ddots & \vdots \\ c_{n1} & c_{n2} & \cdots & c_{nn} \end{bmatrix}^2 \tag{5}$$

where superscripts 1 and 2 correspond to the moving body and stationary body, respectively, and c_{ik} is the influence coefficient of contact pair i due to a unit force located at a contact pair k. As the contact is assumed to be frictionless, the only deformation needed is the one normal to the surface. It is assumed that both bodies are both elastic half spaces, where the contact width is small in comparison to the body dimensions, unless there is a contact scenario, as shown in Fig. 2, where the flat body has a finite length, L, in the axial direction, which can be treated as an elastic finite space [48,49]. The half space model is based on Love's [50,51] explicit solution of the Boussinesq and Cerruti [47] model for a normal deflection due to a uniform pressure applied to a rectangular area $2a \times 2b$ at a general point (x,y) from where the pressure is applied, where the influence coefficient for the contact surface is defined by the following:

$$\begin{aligned} c_{ik} = \frac{\delta_i}{F_k} = \frac{1-\nu^2}{4\pi Eab}\Bigg\{ &(x+a)\ln\left[\frac{(y+b)+\left\{(y+b)^2+(x+a)^2\right\}^{\frac{1}{2}}}{(y-b)+\left\{(y-b)^2+(x+a)^2\right\}^{\frac{1}{2}}}\right] \\ &+(y+b)\ln\left[\frac{(x+a)+\left\{(y+b)^2+(x+a)^2\right\}^{\frac{1}{2}}}{(x-a)+\left\{(y+b)^2+(x-a)^2\right\}^{\frac{1}{2}}}\right] \\ &+(x-a)\ln\left[\frac{(y-b)+\left\{(y-b)^2+(x-a)^2\right\}^{\frac{1}{2}}}{(y+b)+\left\{(y+b)^2+(x-a)^2\right\}^{\frac{1}{2}}}\right] \\ &+(y-b)\ln\left[\frac{(x-a)+\left\{(y-b)^2+(x-a)^2\right\}^{\frac{1}{2}}}{(x+a)+\left\{(y-b)^2+(x+a)^2\right\}^{\frac{1}{2}}}\right] \end{aligned} \tag{6}$$

where E is the Young's modulus and ν is the Poisson's ratio of the body and the compliance matrix can be populated in Eq. (5). For a body that has to be modeled as a finite space, the subsurface stresses are influenced by the free faces and therefore, these free faces at the edges of contact have to be treated as a quarter space. This can be modeled explicitly by the concept of overlapping orthogonal half spaces, where one is in the plane of the contact surface and the other is the plane of the free face, which are discretised into a rectangular grids [52,53]. The normal stress distribution on each of these surfaces (where shear stresses were found to be negligible and therefore, neglected [48]) are related to the pressure of the orthogonal half spaces which can be described by Love's [50,51] explicit solution for the stresses due to a uniform pressure applied to a rectangular area. Equilibrium is then found based on boundary conditions for contact pressure on the contact zone and no load applied to the free faces. A compliance matrix can then be developed based on these conditions, where the details of the full solution is expressed in the works of Zhang et al. [48] and Stan et al. [49].

The problem was formulated for the MSM, where artificial variables, Z_i, were added to the solution to satisfy the constraints. The objective of the problem was to minimizing the following:

$$\sum_{i=1}^{M_xM_y+1} Z_i \tag{7}$$

where the problem can be defined by:

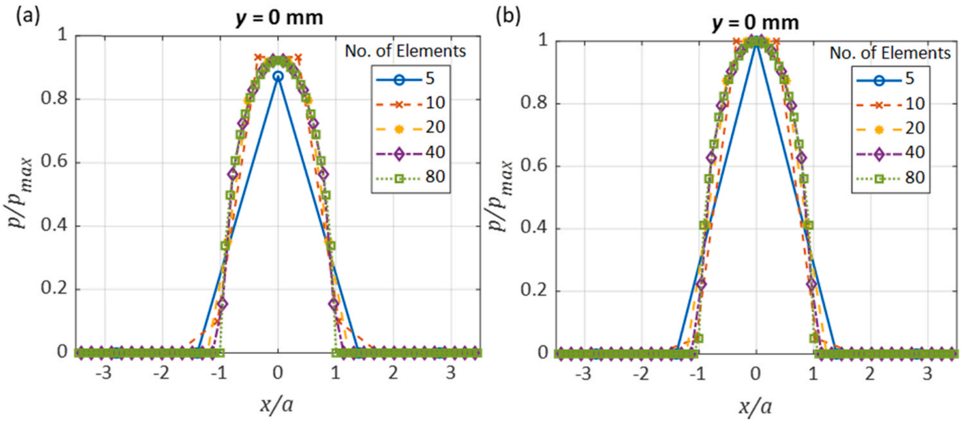

Fig. 3. Mesh convergence of p/p_{max} against x/a for a defined non-dimensionalised contact domain of 7 in the x-direction for (a) a cylinder on flat contact and (b) ball on flat contact.

Table 1
Resulting converged element size in the x-direction for four different examples based on using $7a/40$ ($L = 10$ mm, $E = 200$GPa and $\nu = 0.3$).

Case no.	1	2	3	4
Geometry set up	Cylinder on flat	Cylinder on flat	Cylinder on flat	Ball on flat
$\boldsymbol{R}$ (mm)	6	6	80	6
$\boldsymbol{P}$ (N)	185	500	185	185
$\boldsymbol{a}$ (mm)	0.036	0.059	0.131	0.196
Element size in $\boldsymbol{x}$ (μm)	6.28	10.30	22.92	34.37

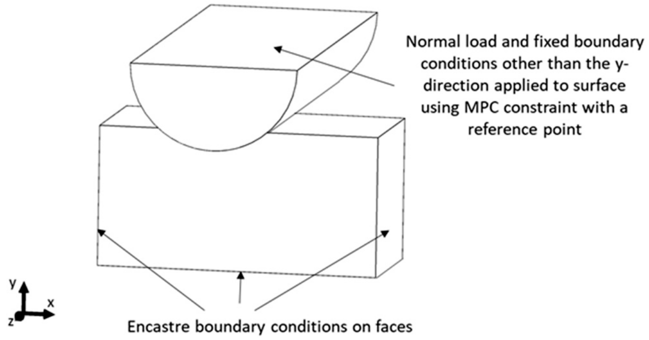

Fig. 4. Load and boundary conditions for the FEA of a cylinder on flat.

$$\begin{aligned}&-\boldsymbol{CF}+\alpha\boldsymbol{e}+\boldsymbol{IY}+\boldsymbol{IZ}=\boldsymbol{\varepsilon}\\&\boldsymbol{e}^T\boldsymbol{F}+Z_{M_xM_y+1}=P\\&F_i\geq 0, Y_i\geq 0, \alpha\geq 0 \text{ and}, Z_i\geq 0.\\&\text{Subject to the criterion of contact, where } F_i=0 \text{ or } Y_i=0\end{aligned} \tag{8}$$

where α is the scalar rigid body approach, $\boldsymbol{e}$ is a unit vector, $\boldsymbol{Y}$ is a vector of all the final separations, $\boldsymbol{I}$ is the identity matrix, $\boldsymbol{\varepsilon}$ is a vector of all the initial separations and $\boldsymbol{e}^T$ is the transpose of the unit vector. The initial separations and the applied load are the inputs, while the contact forces, rigid body approach and final separations are the outputs. The MSM was used to minimize the artificial variables in order to satisfy the constraints and equilibrium with the modification to include the criterion of contact. The details and steps for this algorithm for contact problems are outlined by Vijayakar et al. [41], where a solution is always found.

2.1.1. Grid convergence

A grid convergence study of the rectangular elements was carried out for the contact solver, in order to optimize the use of the refinement methodology. This was performed for a cylinder on flat, shown in Fig. 2, and for a ball on flat. The initial separation of a contact pair was defined by:

$$\varepsilon_i=\frac{1}{2R}x_i^2 \tag{9}$$

$$\varepsilon_i=\frac{1}{2R}\left(x_i^2+y_i^2\right) \tag{10}$$

for the cylinder on flat and ball on flat, respectively, where R is the radius and x_i and y_i are the coordinates for the contact pair, as shown in Fig. 2.

Fig. 3 shows the grid convergence for both cases of the non-dimensionalised contact pressure (contact pressure divided by the maximum contact pressure, p/p_{max}) with respect to the non-dimensionalised x-direction (x coordinate divided by the Hertzian half contact width, x/a) for a non-dimensionalised contact domain of 7 in the x-direction for both cases. It can be seen that the maximum pressure is not located at.

$y = 0$ mm for the cylinder on flat and it is located here for the ball on flat. For both geometry set ups, it can be seen that these both converge between 40 and 80 elements. Using 40 elements as an appropriate value for convergence, the element size in the x-direction for convergence can be found for various cases using $7a$, which are shown in Table 1, due to the Hertzian contact width being based on the geometry and loading. Similarly, convergence in the y-direction for the cylinder on flat cases were 370 μm due to the same value of L and for the ball on flat was equivalent to the element size in the x-direction.

A three dimensional FEA was performed as a benchmark for the contact solver using the geometry shown in Fig. 2 based on parameters of case number 1 in Table 1, where the axial length of the cylinder was 30 mm and the depth of the flat was 10 mm. The load was applied by using a half cylinder and applying a load to the top surface using a multi-point constraint (MPC) with a reference point and using fixed boundary conditions other than the y-direction illustrated in Fig. 4. The flat also had fixed boundary conditions on the left, right and bottom faces, as shown in the schematic. The element size around the contact was 6.28 μm × 370 μm for both the flat and the cylinder and linear brick elements were used (C3D8R). Contact was defined using a surface to surface contact interaction, where the cylinder was chosen as the slave and was set to frictionless. The resulting contact pressure distribution from the FEA and the model is shown in Fig. 5(a) and (b), respectively. It shows that the model has a good agreement with the FEA results with the peak pressure at the center of the x-direction and at the edges of contact in the y-direction. The FEA show a slightly wider contact width by an extra element, i.e. 6.28 μm, either side of the contact width.

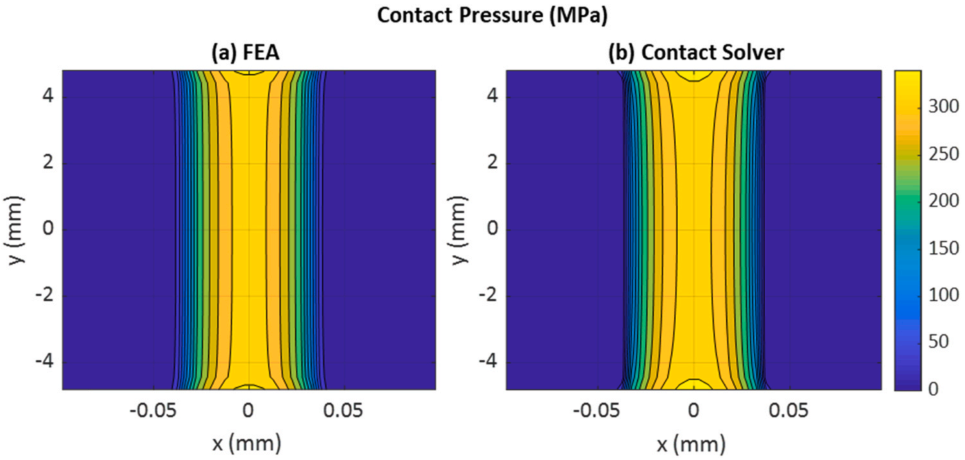

Fig. 5. Contour plots of contact pressure using (a) FEA and (b) the contact solver ($R = 6\text{mm}, L = 10\text{mm}, P = 185\text{N}, E = 200\text{GPa}$, and $\nu = 0.3$).

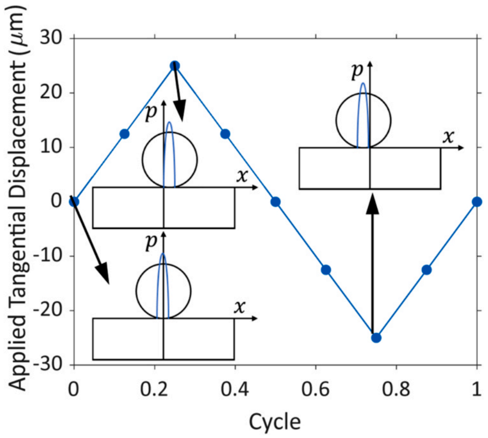

Fig. 6. Applied tangential displacement over one cycle.

2.1.2. Reducing computational time

As the grid is refined, the number of elements increase and, as a result, the computational time increases exponentially. Therefore, a technique has been developed to reduce computational time with grid refinement. The steps of the refinement are as follows:

1. The contact forces were solved for a relatively coarse grid compared to the grid found from the grid convergence using the contact solver. The coarse grid was defined as an element size where the contact pressures, which were solved by this methodology, had a mean absolute percentage error (MAPE) of less than 10% and a coefficient of determination (R^2) close to 1 in comparison with the contact pressures from the element size determined from the grid convergence study.
2. The contact forces were transformed from a vector to a matrix, where the number of columns, M_x, is the number of contact forces in the x-direction and the number of rows, M_y, is the number of contact forces in the y-direction.
3. The contact forces were weighted by dividing by the sum of the contact forces, F_{wj}, in each M_x column in the x-direction of the grid and multiplying by the number of columns. The weightings were as follows:

$$W_{wj} = \frac{F_{wj} M_x}{\sum_{1}^{M_y} F_{wj}} \tag{11}$$

where W_{wj} is the weighting, where subscript w, j is the node location of interest in the x and y direction, respectively, and M_y is the number of rows in the y-direction. The columns are refined, M_x^r, based on a chosen grid refinement and the weightings are refined, W_{wj}^r, by Akima interpolation and extrapolation. The contact forces were found by:

$$F_{wj} = \frac{W_{wj}^r}{M_x^r} \sum_{1}^{M_y} F_{wj} \tag{12}$$

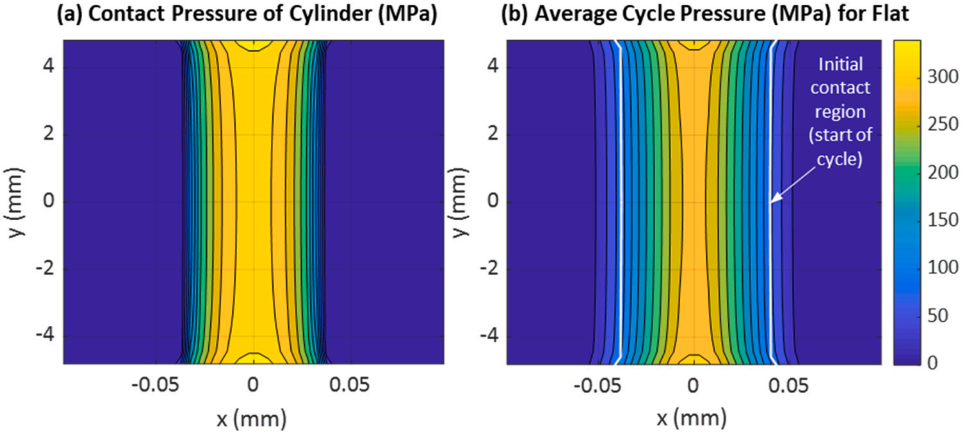

Fig. 7. Contour plots of (a) contact pressure on the cylinder surface and (b) average contact pressure on the flat surface ($R = 6\text{mm}, L = 10\text{mm}, P = 185\text{N}, ds = 25\mu\text{m}$, $E = 200\text{GPa}$, and $\nu = 0.3$).

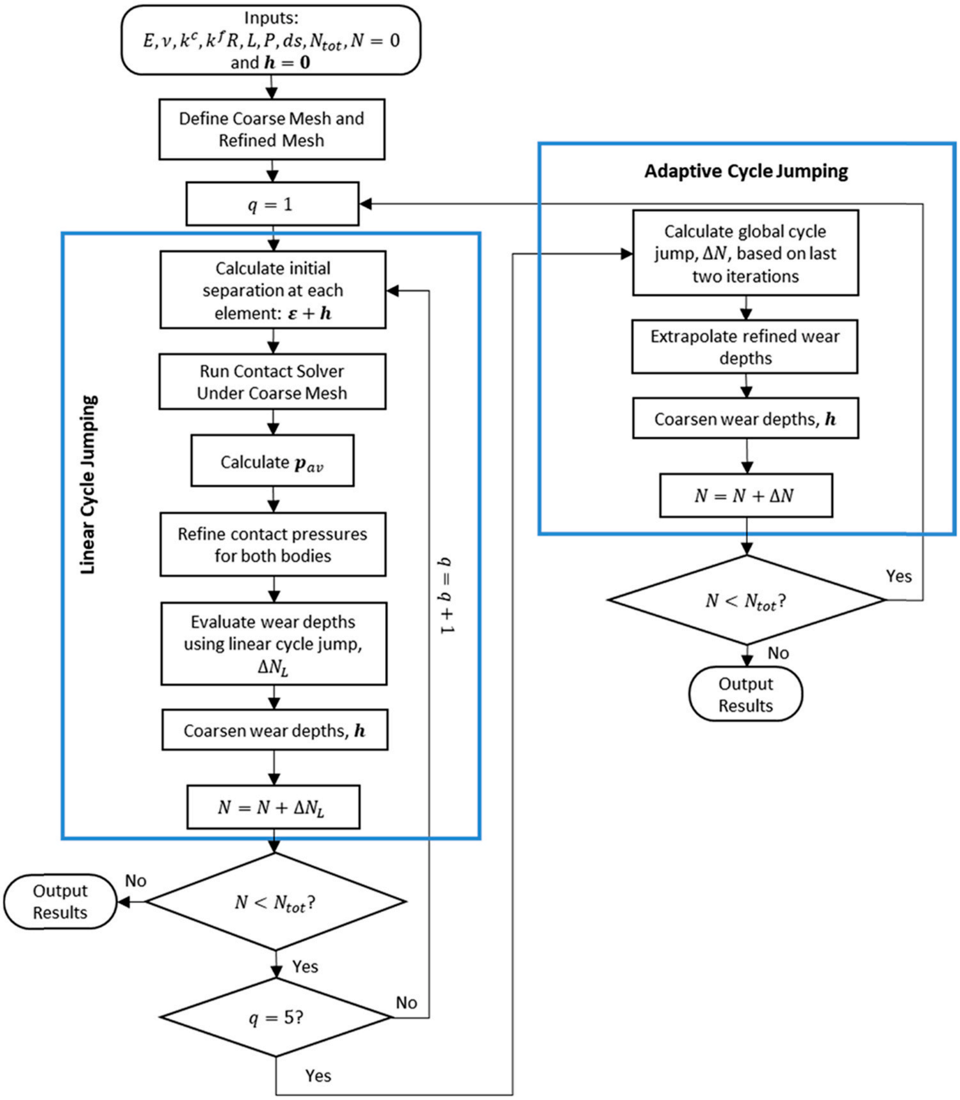

Fig. 8. Detailed flowchart of the overall simulation methodology for predicting fretting wear including cycle jumping and the refinement methodology, where N is the current cycle number.

4. M_y rows for the contact forces in the y-direction are refined following the same method in step 2
5. The grid is refined for all the contact forces and the sum of the contact forces should approximately equal the applied load

The same procedure can also be used to coarsen the grid. This method shall be called the refinement methodology throughout this study and the optimization of this method is discussed in Section 3.1.

2.2. Fretting wear modeling

2.2.1. Average cycle pressure

Due to the relative displacement, during a fretting cycle a single point on the flat contact surface experiences a variation in contact pressure over a displacement cycle, as shown in Fig. 6, resulting in a wider wear scar than just the initial Hertzian contact region alone. In order to obtain the wear scars of the two bodies sufficiently, Andersson et al. [54] introduced the time-averaged pressure on the flat for the numerical simulation of a ball on flat configuration. This was carried out in order to capture the whole contact surface area on the flat. Therefore, following this concept, the average cycle pressure was included for the stationary component in this study, while the cylinder contact pressure profile remains the same. The average pressure that the stationary surface experienced was calculated based on the sliding distance over a cycle. The pressure is calculated over a cycle and at each nodal position the pressure is averaged. Fig. 7 shows an example of a cylinder on flat configuration using case 1 parameters in Table 1 for the model contour contact pressure of a cylinder and the average cycle pressure which the flat experiences over a cycle. For the average cycle pressure for the flat, the pressure is widened due to the pressure experienced over a cycle by the sliding distance and the magnitude of pressure drops due to the average experienced in a cycle, while the cylinder experiences the same contact pressure distribution over a cycle.

2.2.2. Fretting wear

To model fretting wear, Archard's law for sliding wear:

$$\frac{V}{S} = K\frac{P}{H} \tag{13}$$

where V is the wear volume, S is the total sliding distance, K is the dimensionless wear coefficient, P is the applied normal load and H is the hardness of the material, was modified by relating the local incremental wear depth, dh, to the local pressure and local slip amplitudes given by Eq. (14).

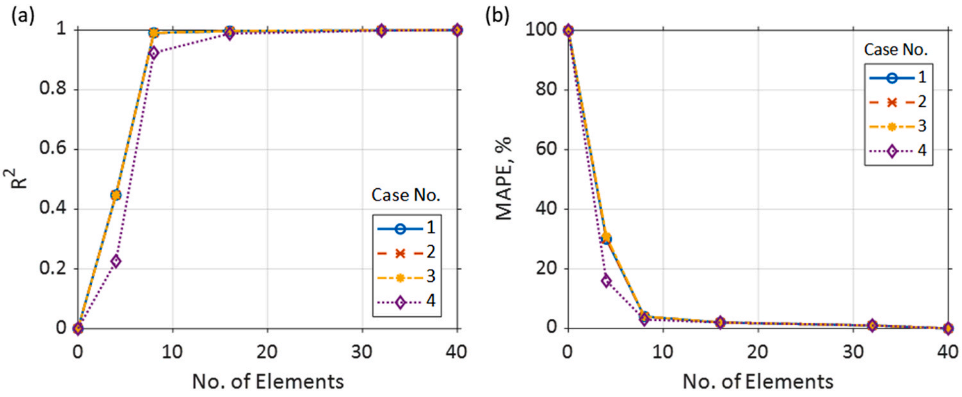

Fig. 9. (a) R^2 and (b) MAPE of the contact pressure distribution against the element size in the x-direction for a coarse grid size using the refinement methodology in comparison with the original contact solver.

$$dh_i = k \bullet \mathrm{p_i} \bullet \mathrm{dS} \tag{14}$$

where k is the wear coefficient, which includes the hardness, p_i is the contact pressure of a node and dS is the total sliding distance during an increment. This was applied to the fretting wear of a cylinder on flat with a linear cycle jump to speed up simulation time, initially implemented by McColl et al. [18]. The incremental wear depths for the cylinder and flat were, therefore, given by the following:

$$dh_i^c = k^c \bullet \Delta \mathrm{N_L} \bullet \mathrm{p_i} \bullet 4\mathrm{ds} \tag{15}$$

$$dh_i^f = k^f \bullet \Delta \mathrm{N_L} \bullet \mathrm{p_{av,i}} \bullet 4\mathrm{ds} \tag{16}$$

where dh^c is the wear depth for the cylinder, dh^f is the wear depth for the flat, k^c is the wear coefficient for the cylinder, k^f is the wear coefficient for the flat, ΔN_L is the linear cycle jump, 4ds is the total sliding distance in a cycle and $p_{av,i}$ the average cycle pressure on the flat surface. The total wear depth at each node, h_i, is the sum of the incremental wear depths of both the cylinder and flat for the current number of cycles, N, given by Eq. (17).

$$h_i = \sum_0^N \left(dh_i^c + dh_i^f \right) \tag{17}$$

The incremental wear depth was calculated for all contact pairs and was added to the initial separation, as shown in Eq. (18). Hence, the contact forces were evaluated with a changing contact geometry and the constraint from equation (8) became the following:

$$-\boldsymbol{CF} + \alpha\boldsymbol{e} + \boldsymbol{IY} = \boldsymbol{\varepsilon} + \boldsymbol{h} \tag{18}$$

where $\boldsymbol{h}$ is a vector of the total wear depths for all contact pairs.

2.2.3. *Adaptive cycle jumping*

In order to further reduce the computational time of the wear simulation, an adaptive cycle jumping technique was implemented in the model, this allowed the wear depth, h, of both bodies to be calculated at a reduced number of cycles throughout the simulation, improving the computational efficiency. The adaptive cycle jumping technique used was based on that previously implemented for low cycle fatigue [55,56]. To determine the cycle jump needed, the wear depths after a cycle jump ($N + \Delta N$) were formed based on the 2nd order Taylor series expansion as follows:

$$h_{N+\Delta N} = h_N + \dot{h}_N \Delta N + \frac{\ddot{h}\Delta N^2}{2} + \dots \tag{19}$$

where ΔN is the cycle jump; $\dot{h}$ and $\ddot{h}$ are the first and second derivatives, respectively, of the wear depths. These derivatives were calculated by the backward finite difference scheme, which is given by the following:

$$\dot{h}_N = \frac{h_N - h_{N-\Delta N_L}}{\Delta N_L} \quad \text{and} \quad \ddot{h}_N = \frac{h_{N-2\Delta N_L} - 2h_{N-\Delta N_L} + h_N}{\Delta N_L^2} \tag{20}$$

This uses linear cycle jumping which ran for $q = 5$ successive iterations, where the first 3 iterations were used for stabilization [56] and the last two iterations were used to determine the derivatives for extrapolation. The cycle jump size was determined by minimizing the first order of the Taylor series, as the second order is negligible compared to the first, given by Eq. (21).

$$\left|\dot{h}_N\right| \Delta N \le \eta |h_N| \quad \rightarrow \quad \Delta N = \eta \frac{|h_N|}{\left|\dot{h}_N\right|} \tag{21}$$

where η is the accuracy parameter for neglecting the higher order terms. This cycle jump was calculated for the wear depths at all elements for both bodies and the minimum cycle jump size was chosen. This cycle jump was also bounded by a maximum cycle jump size, ΔN_{max}. The wear depths were then extrapolated using Eq. (19) for $N + \Delta N$ cycles. A Design of Experiment (DOE) was performed to determine the optimal values of η, ΔN_{max} and the linear cycle jump, ΔN_L considering the effects on solution time and accuracy.

The refinement methodology was used for the coarsening of the grid for wear depths, where conservation of the wear volume was ensured, which was input into the contact solver. The detail of the implementation of the cycle jumping and refinement methodology is shown in Fig. 8.

3. Results and discussion

Studies were carried out to optimize computational time using the refinement and cycle jumping methodologies. Validation of fretting wear depths and wear scars were also compared with previous FEA and experimental results from previous literature, as well as a comparison of computational times when compared with FEA and BEM.

3.1. *Computational time optimization*

From the grid convergence study, the converged number of elements in the x-direction for a proposed contact region 7a was 40 for a cylinder on flat and ball on flat configuration. To determine the coarse mesh for the refinement methodology, the number of elements was varied from 4 elements up to 40 elements and compared with the solution without the refinement methodology. This was performed for the cases outlined in Table 1, where Fig. 9 shows the coefficient of determination (R^2) and the mean absolute percentage error (MAPE) for the contact pressure as the coarse grid is refined in the x-direction for the refinement solver for the 4 cases. The closer R^2 is to 1 shows a good correlation between the contact solver and the interpolation solver, whereas a lower value of MAPE

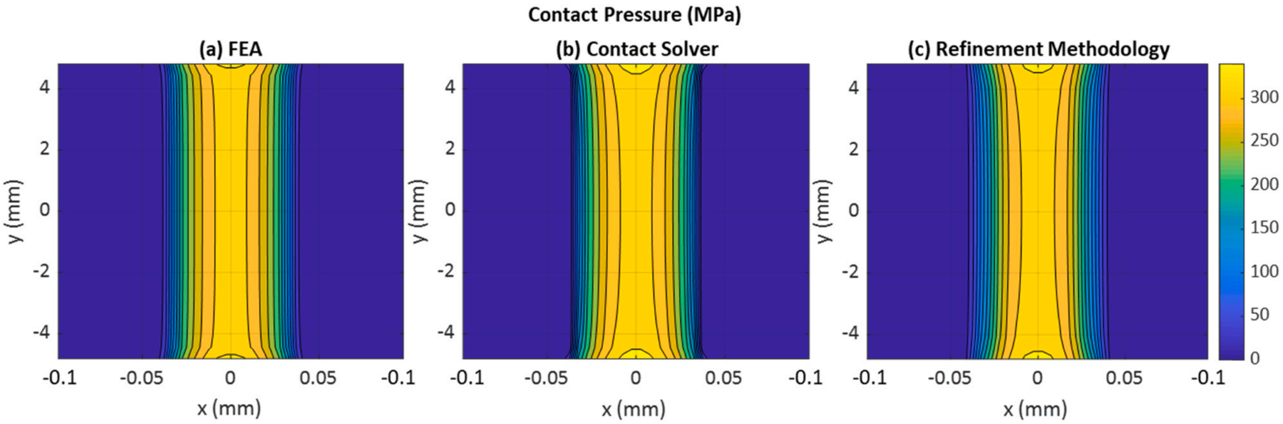

Fig. 10. Contour plots for case number 1 of (a) the cylinder contact pressure using the contact solver for a 6.3 μm × 370 μm element size and (b) the refinement solver for a 15.75 μm × 1000 μm element size refined to a 5 μm × 370 μm element size ($R = 6\text{mm}$, $L = 10$ mm, $P = 185$ N, $E = 200$ GPa, and $\nu = 0.3$).

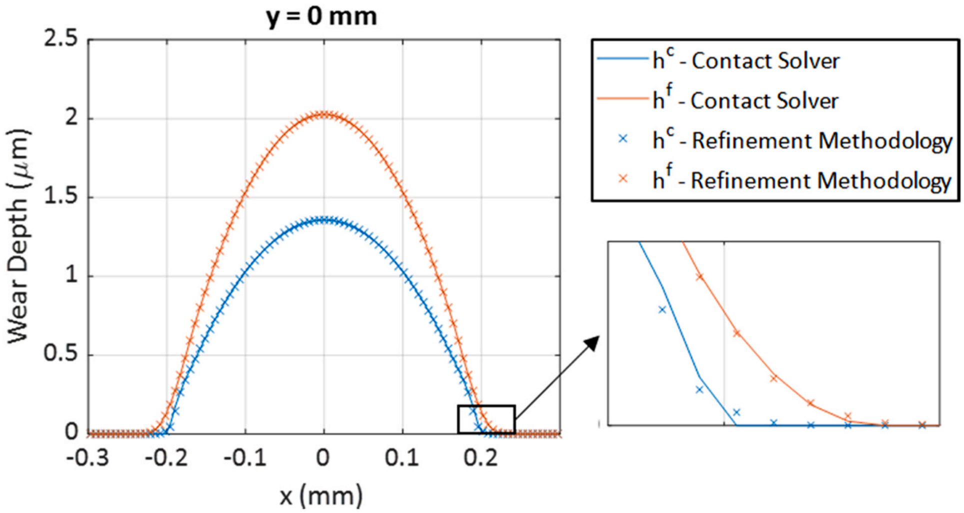

Fig. 11. Wear scars for the cylinder and flat after 10,000 cycles using the contact solver for a 6.3 μm × 370 μm element size and with the refinement methodology for a 15.75 μm × 1000 μm element size with no cycle jumping ($R = 6\text{mm}, L = 10$ mm, $P = 185$ N, $ds = 25\mu\text{m}, E = 200\text{GPa}$, $\nu = 0.3$, $k^c = 2 \times 10^{-8}$ MPa^{-1} and $k^f = 3 \times 10^{-8}$ MPa^{-1}).

shows a lower percentage error between the refinement solver contact pressure values and the actual values from the contact solver. As the number of elements increase to the actual mesh refinement size, the R^2 value tend towards 1 and the MAPE value tend towards 0%. This was performed for the coarse mesh element size for the *y*-direction as 1000 μm for the cylinder on flat cases and equivalent mesh size with the *x*-direction was used for the ball on flat, which maintained a high R^2 value and a low MAPE of 1.61% with respect to the original mesh. It can be seen in Fig. 9 for the cylinder on flat cases (1-3), the R^2 values follow the same trend due to the set up being the same and the proposed contact zones being proportional based on the loading and radius change, while the ball on flat case (4) differs slightly due to this being a different distribution of load, but overall follows the same trend. For the MAPE, the trend is the same for all cases, but the values differ slightly due to the refinement methodology leading to the contact width varying and therefore, the pressure varies more at the edges of contact affecting the overall MAPE. From these plots, it can be seen for all cases that the minimum number of elements that can be used for the coarse grid was 16, which gave a high correlation and a MAPE that fell below 10%. This is 2.5 times the actual mesh size and gave an average of 98% reduction in time using the refinement methodology.

A comparison using case 1 of the contact pressure distribution using FEA, the actual mesh using the contact solver and the use of the refinement methodology are shown in Fig. 10. It can be seen that by using the refinement methodology, the pressure does not vary in the *y*-direction in comparison to without the refinement methodology due to the finite length; however in the *x*-direction, the contact width widens due to being based on a coarser mesh, which becomes similar to the FEA. Overall, the refinement methodology contact pressure still provides a good agreement with the FEA and the contact solver. The FEA took 3 h 15 min to run due to the refined mesh and being in three dimensions, while the contact solver and refinement methodology took 14.7 s and 0.35 s, respectively, giving a significant reduction in time.

The effect of the refinement methodology on the fretting wear results was investigated using case 1 for 10,000 cycles with a tangential displacement of 25 μm. The results for the wear depths for the cylinder and flat at $y = 0$ mm are shown in Fig. 11. It can be seen that the results correlate well with results without the use of the refinement methodology with minor differences (with respect to the overall wear scar) in the wear scar widths, which were 10 μm and 20 μm for the flat and cylinder, respectively, due to the refinement methodology being based on a coarser mesh. As the computational efficiency of the fretting wear model is highly dependent on the contact solver, it was found there was a 98.9% reduction in simulation time through using the refinement methodology.

Following from this, the cycle jumping methodology was optimized to reduce the simulation time further. Firstly, the linear cycle jump has

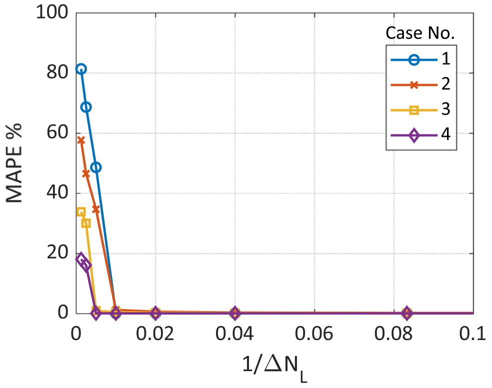

Fig. 12. Variation in the percentage error between the total wear depth at the center of the contact region after 10,000 cycles with $ds = 25$ μm for different ΔN_L in comparison with $\Delta N_L = 1$ for 4 example cases.

Table 2
Levels chosen for each factor required for the DOE.

Factors/levels	-1	0	1
η	0.1	0.55	1
ΔN_{max} (Cycles)	100	345	600
ΔN_L (Cycles)	10	55	100

to be optimized, as stability issues arise if the cycle jump is too high [57]. This was achieved by comparing the final contact pressure distribution after 10,000 cycles with various linear cycle jumps with the results from no cycle jumping by calculating a MAPE. Examples have been performed for all 4 cases from Table 1 for a tangential displacement of 25 μm and the MAPE results with respect to the inverse of the cycle jump are shown in Fig. 12. It can be seen that as the size of the cycle jump increases, there is a maximum value cycle jump before instability occurs and the MAPE increases for all cases. It was found that the stability issues arose for linear cycle jumps higher than 100 for case numbers 1 and 2, and 200 for case numbers 3 and 4. These were chosen as the maximum linear cycle jump to be used for the DOE of the adaptive cycle jumping parameters.

Three factors were chosen for the DOE, which were the accuracy factor, the maximum cycle jump and the linear cycle jump and three levels were chosen for each of these (−1, 0 and 1), which are shown in Table 2. Fig. 13 shows the results from the DOE which presents the mean values of the time and the MAPE between the total wear depths with no cycle jumping and with cycle jumping varying with the diffrent factor-levels. It can be seen that the time decreases as all the factors get larger. It can also be seen that the MAPE gets larger for increasing factors of η and ΔN_{max}, whereas the minimum MAPE for ΔN_L was found to be the intermediate case of 55 cycles. It was also found that the coefficient of determination was always greater than 0.99 for the total wear depths, when compared with no cycle jumping. To ensure stability and to achieve the lowest MAPE, an accuracy factor of 0.55, a maximum cycle jump of 600 and a linear cycle jump of 55 were chosen to optimize the computational time. Using these parameters, the maximum total wear depth plotted against the number of cycles is shown in Fig. 14, which presents the cycle jumping technique. A comparison of the wear depths for the cylinder, h^c, and flat, h^f, across the center of its length for no cycle jumping and with adaptive cycle jumping are shown in Fig. 15. The wear depths showed an excellent agreement with results found without cycle jumping techniques, while reducing the simulation time.

3.2. Validation of wear modeling

Initially, simulations were performed with the current 3D simulation method using the parameters from McColl et al. [18] for a 2D cylinder on flat fretting wear simulation. The parameters were the same as case 1 with a tangential displacement of 25 μm for a Super CMV cylinder and a

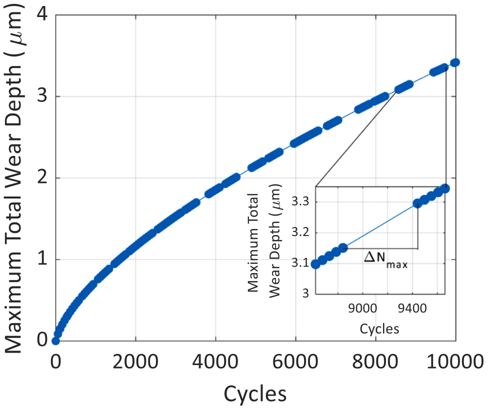

Fig. 14. The maximum total wear depth in comparison with the number of cycles.

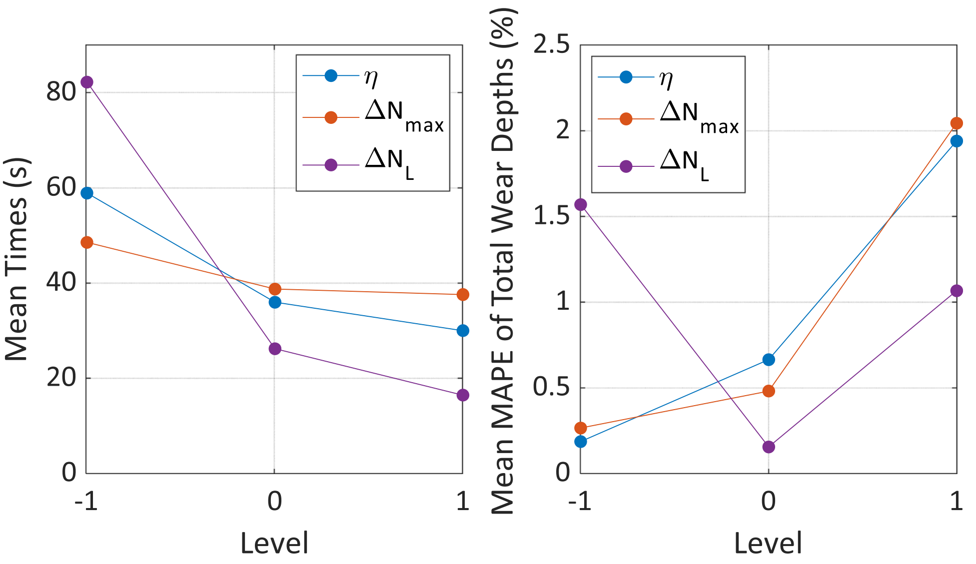

Fig. 13. Plots of the mean times and MAPE of the total wear depths from the DOE for 3 levels.

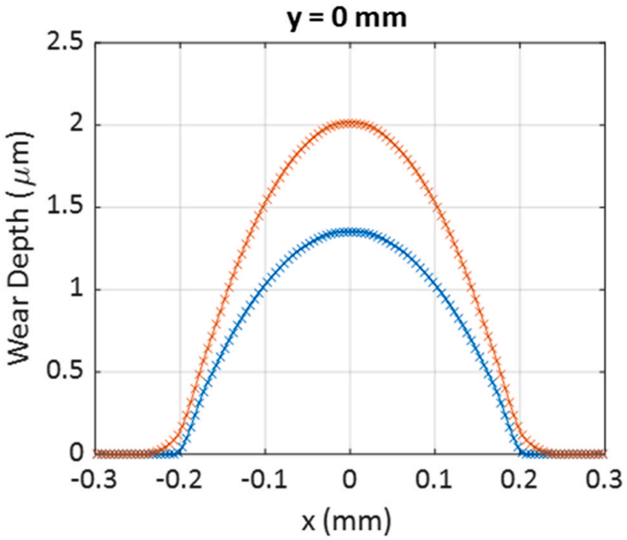

Fig. 15. Wear depths of the cylinder and the flat without a cycle jump and with adaptive cycle jumping technique ($N = 10,000$, $\eta = 0.55$, $\Delta N_{max} = 600$ and $\Delta N_L = 55$).

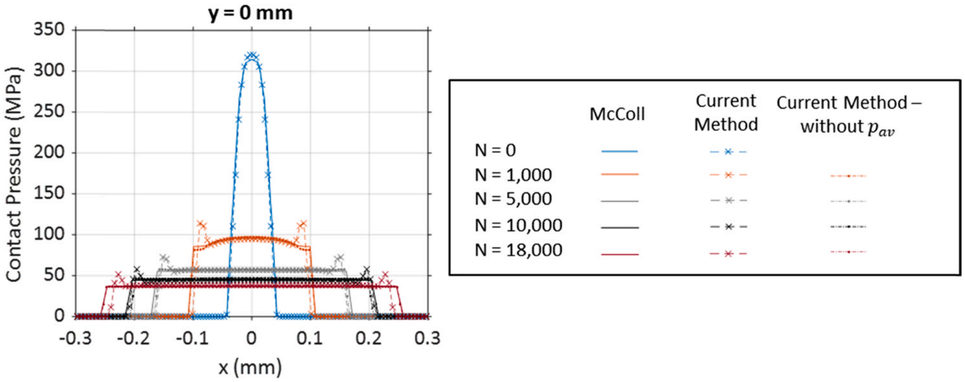

Fig. 16. A comparison between the current model and McColl et al.'s [18] FEA simulation for the contact pressure distributions across the center of the length.

nitrided Super CMV flat, where the wear coefficients for the cylinder and flat were 2×10^{-8} MPa^{-1} and 3×10^{-8} MPa^{-1}, respectively.

Pressure distributions and wear profiles across the center of the length ($y = 0$ mm) at 1000, 5000, 10,000 and 18,000 cycles are presented in Fig. 16 and Fig. 17, respectively, compared with the FEA simulation results of McColl et al. [18]. In Fig. 16, it can be seen that the central peak pressure reduces as the contact area becomes wider due to the removal of material as the number of cycles increase. Also, the plot shows that the center of the pressure distributions from the FEA and the current simulation follow similar values and trend with an increasing number of cycles; however, the current simulation gives pressure peaks at the edge of contact due to the addition of the average cycle pressure for the flat stationary component. This changes how the edges of contact interact with each other, an example of which can be seen for a loaded contact after 1000 cycles without average cycle pressure and with average cycle pressure in Fig. 18. The wear depth of the flat causes a gradual profile transition of the wear with average cycle pressure compared to those without. This causes the cylinder worn profile edges to embed into the worn flat surface giving pressure peaks at the edges, whereas without averaging the cycle pressure, the cylinder worn profile slots into the worn profile edge to edge. Furthermore, the wear depth at $y = 0$ mm, shows a similar trend for all three solutions, but the current method with and without the average cycle pressure show very similar results in terms of the magnitude of tbe wear depths. It can be seen that the solution with the average cycle pressure has a wider wear scar width than without, as expected, due to the latter not taking into account the contact pressure over the sliding distance. The wear depths from the FEA show a lower wear depth for the cylinder and more for the flat in comparison with the current method, which can be explained due to the FEA taking into account the coefficient of friction, which was 0.9, whereas the current model does not take this into account. The FEA slip distribution is calculated based on this and this evolves with slightly with wear [57], whereas the current method assumes uniform slip across the contact throughout the simulation. As the modified Archard's wear law equation is dependent on the local slip, then this will cause a difference in the overall solution. Despite this, the current method shows a reasonable agreement with the FEA for the bulk fretting wear simulations under gross slip.

Computational time for this simulation are compared with the FEA modeling of McColl et al. [18] and the BEM modeling of Wan Kim et al. [30] in Table 3. The current method uses a combination of grid refinement techniques, linear cycle jumping in conjunction with an adaptive cycle jumping technique. The current method gives a 99.9% and 98% reduction in time for the cylinder on flat contact compared with the FEA with a linear cycle jump and the BEM without any cycle jumping for 18,000 cycles, respectively, despite it being a 3D simulation and having a reduction in element size. For the ball on flat, the current model had a 99.9% reduction in simulation time with respect to the BEM, while being longer in comparison with the cylinder on flat due to the equivalent mesh size in both directions. A larger linear cycle jump was able to be

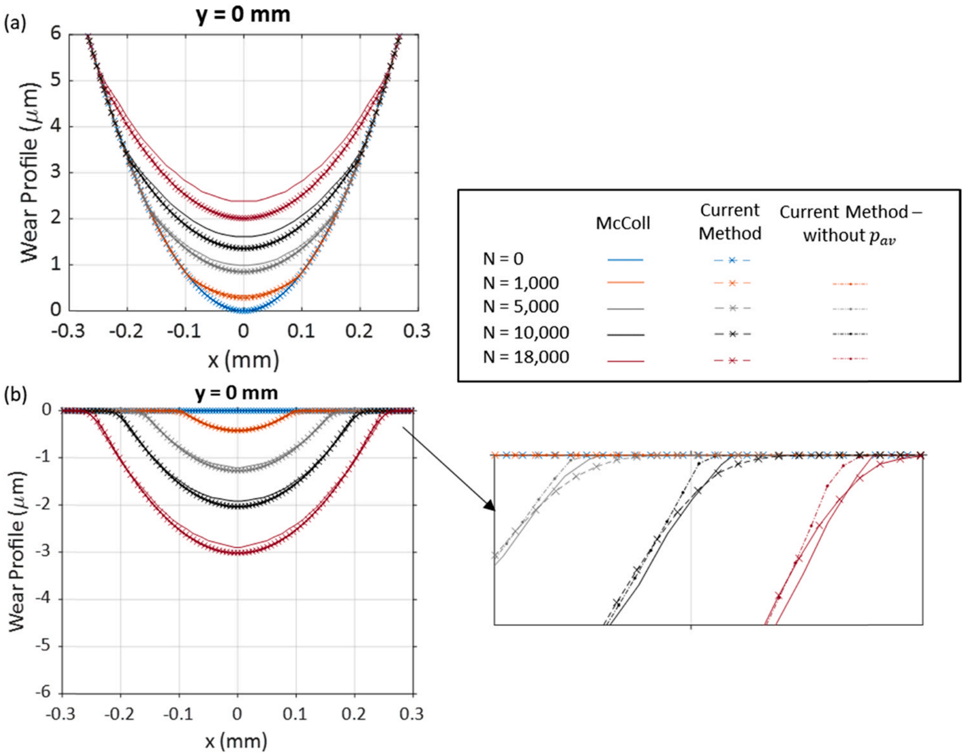

Fig. 17. A comparison between the current model and McColl et al.'s [18] FEA simulation for the wear depths across center of the length for (a) the cylinder and for (b) the flat.

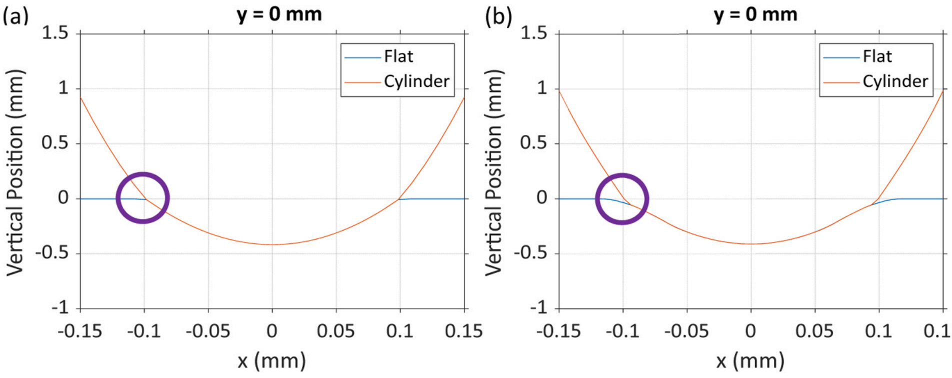

Fig. 18. Changes in the edges of loaded contact for (a) without average cycle pressure and (b) with average cycle pressure.

Table 3
Simulation time comparisons.

Set-up	2D Cylinder on flat	3D Cylinder on flat		3D Ball on flat	
Method	**FEA** [18]	**BEM** [30]	**Current method**	**BEM** [30]	**Current method**
Element size in x (μm)	10	10	6.3	10	6.3
Linear Cycle Jump	30	1	55	1	55
Total Number of Cycles	18,000	18,000	18,000	1000	1000
Number of Iterations	600	18,000	198	1000	20
Simulation Time	1 day	30 min	36 s	10 hr	44 s

used and a smaller number of iterations are required giving the increased reduction in time. With this improvement in computational time, this gives the potential for this method to be used as part of a design tool that allows to design against wear of industrial components.

Furthermore, simulations were run to compare with experimental values and FEA values of wear scars and wear depths from previous literature for cylinder on flat fretting wear tests. All cylinders had a radii of 6 mm and a length of 10 mm. Wear coefficients are either reported in previous literature or found using reported wear volumes using:

$$k = \frac{V}{4ds \bullet P \bullet} N_{tot} \tag{22}$$

All findings for wear scars and maximum wear depths are presented in Table 4. Experimental results show the maximum wear depth from a reduced section within the contact region to take out the end affects and FEA results show results from 2D simulations. It was found that the MAPE for the wear scar widths and depths shown in Table 4 for the FEA, compared with the experimental values, were 15.4% and 23.1%,

Table 4
Wear scars and wear depth of flat in comparison with experimental and FEA results.

Reference		[18]	[18]	[18]	[23]	[58]	[15]	[15]	[15]
Load (N)		185	500	1670	500	250	450	450	450
Tangential Displacement (μm)		25	25	25	10	100	50	50	50
Number of Cycles		18,000	18,000	18,000	18,000	100,000	1,000,000	1,000,000	1,000,000
Frequency (Hz)		20	20	20	20	20	20	100	200
Material of Cylinder		Super CMV	Super CMV	Super CMV	Super CMV	High Strength Steel S132	High Strength Steel S132	High Strength Steel S132	High Strength Steel S132
Material of Flat		Nitrided Super CMV	Nitrided Super CMV	Nitrided Super CMV	Nitrided Super CMV	High Strength Steel S132	High Strength Steel S132	High Strength Steel S132	High Strength Steel S132
Wear Coefficient of Cylinder (MPa^{-1})		2.00×10^{-8}	3.00×10^{-8}	1.50×10^{-8}	2.50×10^{-8}	2.50×10^{-8}	9.93×10^{-9}	6.57×10^{-9}	4.60×10^{-9}
Wear Coefficient of Flat (MPa^{-1})		3.00×10^{-8}	5.50×10^{-8}	3.00×10^{-8}	4.90×10^{-8}	2.50×10^{-8}	9.93×10^{-9}	6.57×10^{-9}	4.60×10^{-9}
Scar Width (mm)	**Experimental**	0.54	0.59	0.75	0.50	–	2.84	2.39	2.10
	FEA	0.52	0.79	0.87	0.54	–	–	–	–
	Current method	0.55	0.87	1.08	0.62	–	2.47	2.21	1.97
Wear Depth (μm)	**Experimental**	2.9	15.0	15.6	5.0	25.0	54.4	38.0	28.9
	FEA	3.0	8.4	11.7	4.0	–	–	–	–
	Current method	3.0	9.0	13.4	4.5	24.4	57.1	43.4	34.2

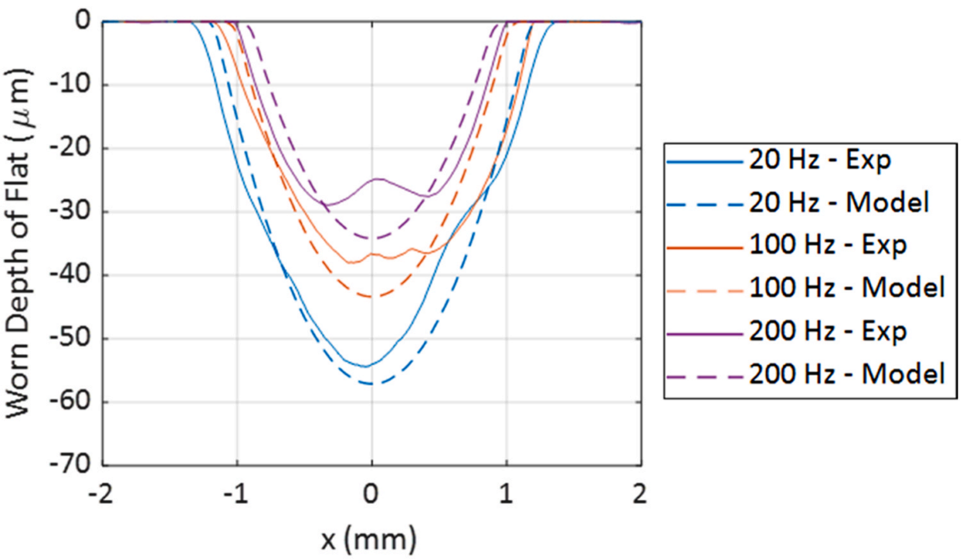

Fig. 19. Average worn depth profiles comparison with the current model and updated experimental results (Exp) [15].

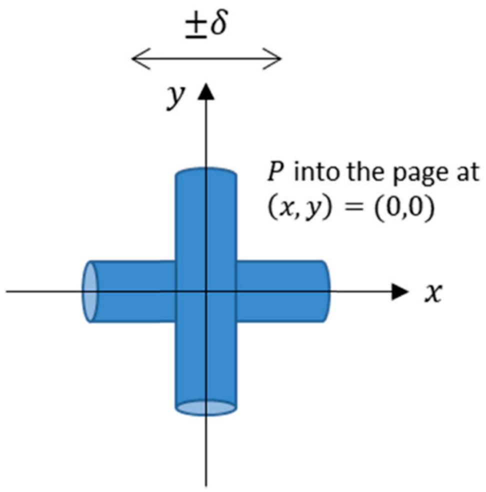

Fig. 20. Schematic of two crossed cylinders and loading.

Table 5
Simulation parameters for fretting wear modeling of wire ropes.

Diameter of cylinders, D (mm)	0.45
Tangential Displacement, $\pm\delta$ (μm)	65
Young's Modulus, E (GPa)	210
Poisson's Ratio, ν	0.3
Normal Load, P (N)	1
Number of Cycles, N_t ($x10^3$)	20
Wear Coefficient (MPa^{-1})[28]	3.545×10^{-8}

respectively, while for the current method, it was 20.1% and 13.4%, respectively. These predictions may differ due to the FEA results being from a 2D simulation and the current method being a 3D simulation with additional techniques to reduce computational time. With the current simulation being in 3D, it will take into account the end affects experienced in the y-direction, where a 2D simulation does not. Additionally, the scar width will vary with the current method due to the refinement methodology predicting the contact width based on a coarsened grid.

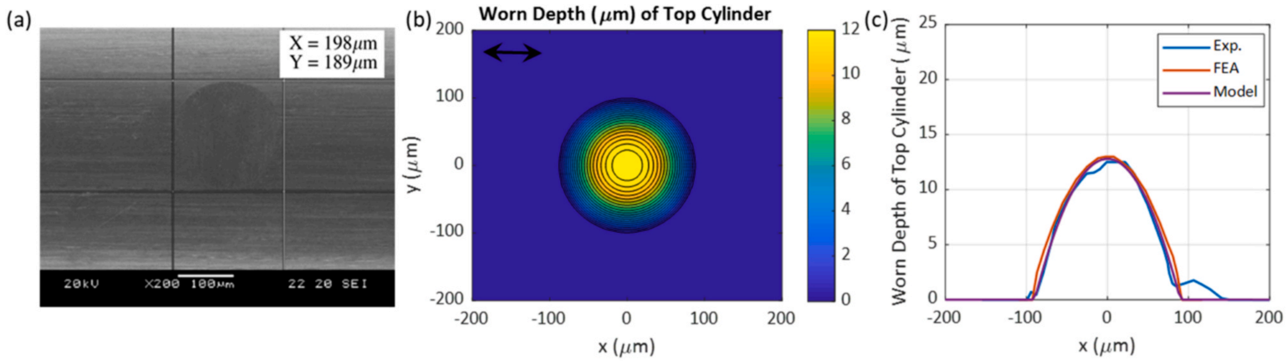

Fig. 21. (a) SEM image of experimental worn scar [28], (b) contour plot of model wear scar and (c) a comparison of the wear profile between the experiment (Exp.) and FEA model by Cruzado et al. [28] and the model for the top cylinder at $y = 0\text{mm}$.

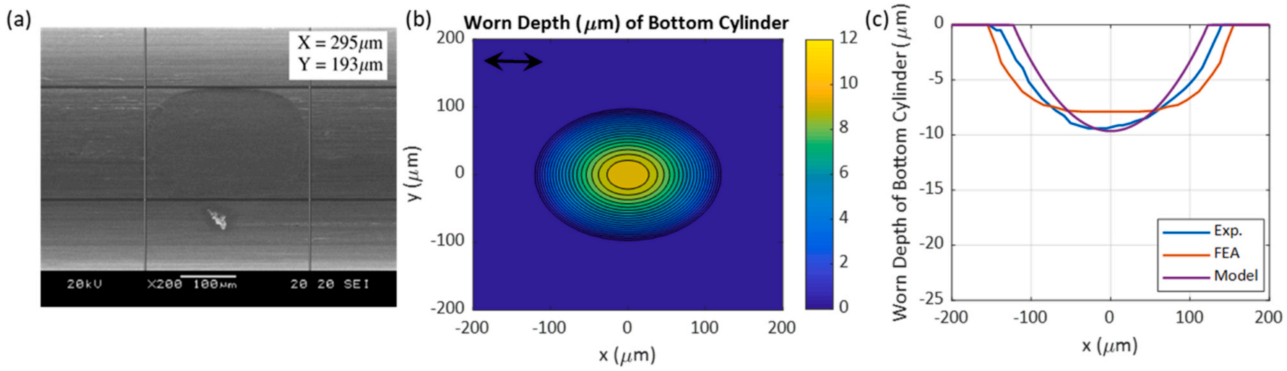

Fig. 22. (a) SEM image of experimental worn scar [28], (b) contour plot of model wear scar and (c) a comparison of the wear profile between the experiment (Exp.) and FEA model by Cruzado et al. [28] and the model for the bottom cylinder at $y = 0\text{mm}$.

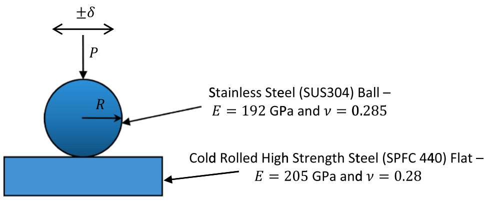

Fig. 23. Schematic of a ball-on-flat, fretting wear loading and material parameters.

Table 6
Geometry and loading for ball-on-flat.

Radius of ball, $\boldsymbol{R}$, (mm)	2.5
Tangential Displacement, $\pm\boldsymbol{\delta}$, (μm)	90
Normal Load, $\boldsymbol{P}$, (N)	50
Number of Cycles, N_t, ($\times10^3$)	4
Wear Coefficient of SPFC 440 (MPa^{-1}) [13]	8.56×10^{-8}
Wear Coefficient of SUS304 (MPa^{-1}) [60]	3.81×10^{-8}

Further errors also may be explained by experimental errors made during the tests. It should be noted that the MAPE for the FEA are not fully comparable as the FEA has been simulated for fewer tests. Overall, the current method was able to make a reasonable prediction of the scar width and scar depth for various numbers of cycles, normal loads and tangential displacements.

Fig. 19 shows experimental results of the average wear depth profiles of the flat [15] for a million cycles for different frequencies for a normal load of 450 N and a tangential displacement of 50 μm, compared with the modelling results. In general, the wear profiles show a good agreement with the experimental results as the plot shows the wear scar widths and the maximum wear depths reduce as the frequency increases; however, as the frequency increases, the model is unable to capture the variation in the wear depths about the center. Kirk [15] found that at 20 Hz an oxide layer covered the whole fretting area and as the frequency was increased this oxide layer reduced and debris entrapment and plastic deformation becomes present. This explains why the model is not able to capture the central wear profile for higher frequencies as it does not take into account these phenomena. Thus, increasing the percentage error (and therefore the MAPE) for the maximum wear depth at 200 Hz.

4. Practical applications

4.1. Steel wire ropes for industrial applications

Steel wire ropes consist of many twisted strands of wires and have many industrial applications such as lifts, cranes and funicular railways [28,29,59]. When the rope runs over wire rope sheaves, this causes small oscillatory movement between the wires inducing fretting wear. This can lead to premature failure of the wires leading to a reduction in the structural integrity of the rope and its life.

Fretting wear of the wires can be modeled as two perpendicular cylinders with a normal load and tangential displacement of the top cylinder, as shown in Fig. 20, where the initial separation is mathematically equivalent for a ball on flat given by Eq. (10) and R is the radius of both cylinders. Cruzado et al. [28] performed experiments and used a FEA based simulation to predict fretting wear scars. A comparison has been made with the simulation parameters presented in Table 5. Cruzado et al. [28] used a different wear coefficient for each cylinder

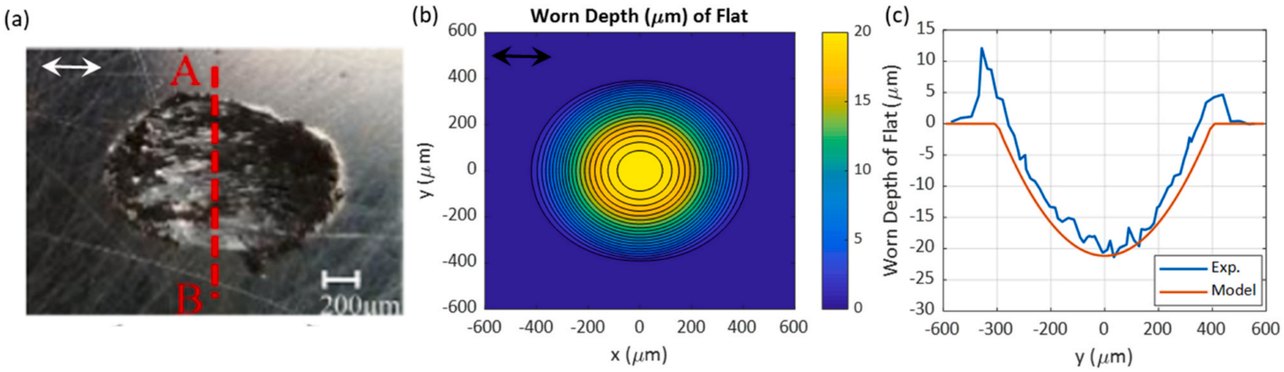

Fig. 24. (a) Image of experimental worn scar of flat [13], (b) contour plot of the model worn scar of flat and (c) a comparison of the worn profiles of flat at $x = 0$ mm between the experiment (Exp.) [13] and model.

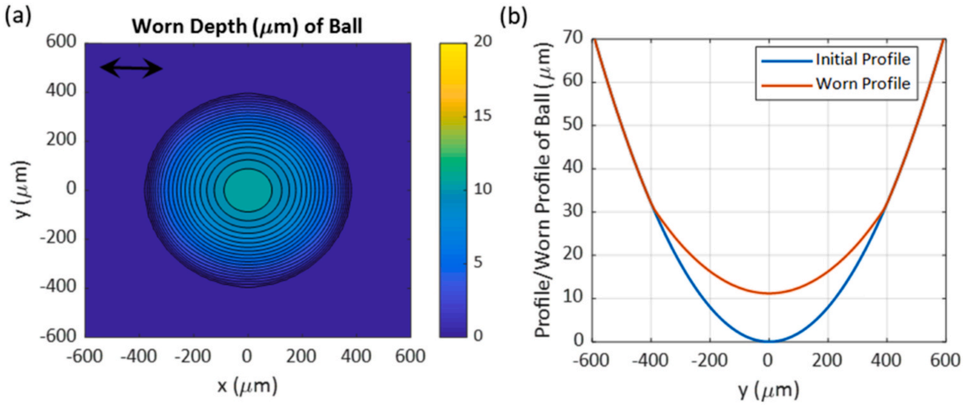

Fig. 25. (a) Contour plot of the model worn scar of ball and (b) the profile and worn profile of the ball at $x = 0$ mm.

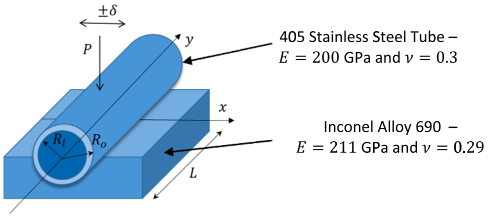

Fig. 26. Tube on flat geometry and loading.

Table 7
Simulation parameters for fretting wear modeling of steam generator tubes.

Outside Radius, R_o (mm)	8.75
Inside Radius, R_i (mm)	7.75
Length of Flat, L (mm)	12
Tangential Displacement, $\pm\delta$ (μm)	100
Normal Load, F (N)	40
Number of Cycles, N_t	10^5
Wear Coefficient for Inconel Alloy 690 at RT[7] (MPa^{-1})	2.27×10^{-8}
Wear Coefficient for 405 Stainless Steel at RT[7] (MPa^{-1})	3.13×10^{-9}
Wear Coefficient for Inconel Alloy 690 at 90 °C[7] (MPa^{-1})	6.09×10^{-8}
Wear Coefficient for 405 Stainless Steel at 90 °C[7] (MPa^{-1})	3.13×10^{-8}

found from the experiment and, therefore, this was averaged for this model simulation.

Results for the top wear scar and the bottom wear scar are presented in Fig. 21 and Fig. 22 respectively.

When observing the wear scar size and shape, the model contour plots for both the top and bottom cylinder show a good agreement with the SEM images. In Fig. 21(c), it was found that the wear profiles of the top cylinder from the model agree well with the FEA results and experimental results. Although, there are slight differences with the experimental wear profile where there is material transfer at the right hand side of the wear scar, this can be explained due to the modified Archard's wear equation not taking into account the debris entrapment and material transfer. For the wear scar on the bottom cylinder, the wear scar size from the experiment in Fig. 22(a) matches well with the wear depth contour in Fig. 22(b). The corresponding wear profiles at $y = 0$ mm shown in Fig. 22(c) show that the model correlates well with the experiment in magnitude and shape, while the FEA model shape differs with a flattening at the center of the wear scar. The width of the wear scar differs due to an average of the wear coefficient used instead of using different wear coefficients for both cylinders unlike Cruzado et al. [28], who used a larger wear coefficient for the bottom cylinder than the top cylinder. Furthermore, the differences with the FEA can be explained by the subroutine, UMESHMOTION, used for the motion of nodes due to local incremental wear. It only gives contact pressure and slip distribution results for the slave surface nodes (defined as the top cylinder) and therefore, an interpolation method was used to interpolate these distributions to the master surface nodes, i.e. the bottom cylinder. Results did vary depending on the interpolation method used and this could be the difference in the overall results. Additionally, the FEA took into account the coefficient of friction of 0.7, which would alter the slip distribution with wear, whereas the current model assumes a uniform slip distribution.

Overall, the modeling methods presented were able to capture the wear scar shape for perpendicular cylinders under fretting wear using a wear coefficient based on the average of the total wear volume from

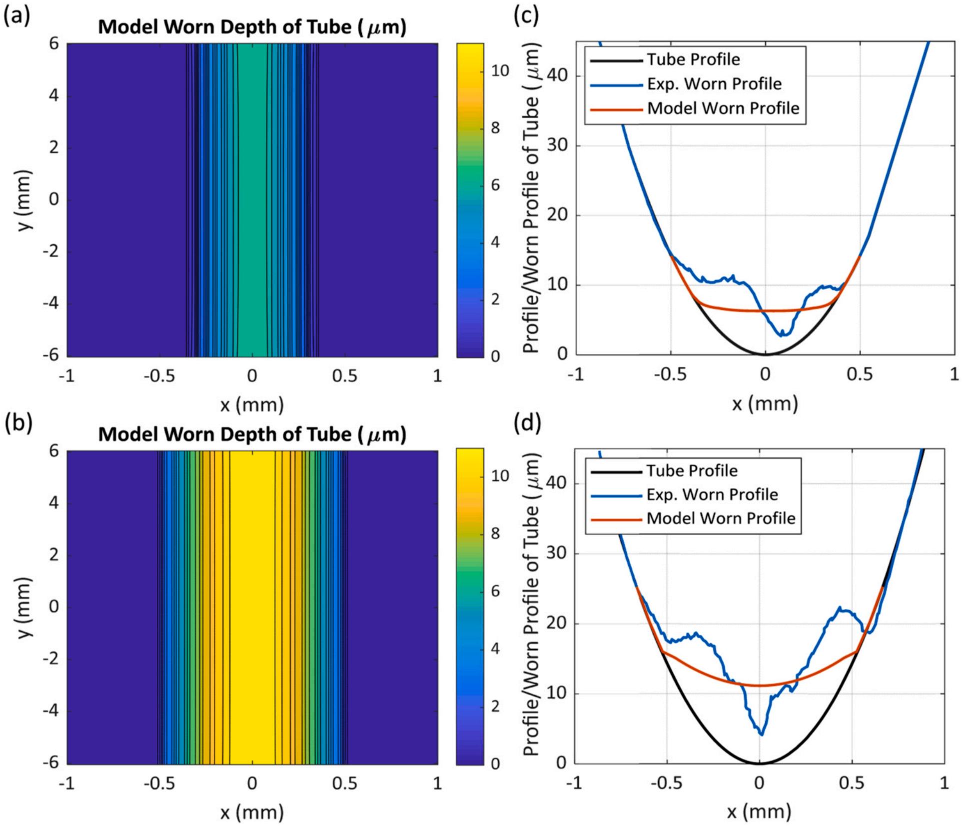

Fig. 27. Worn depth contours of the tube at (a) RT and at (b) 90 °C and worn profile comparisons of the tube (at $y = 0$ mm) with the experiment (Exp.) [7] at (c) RT and at (d) 90 °C.

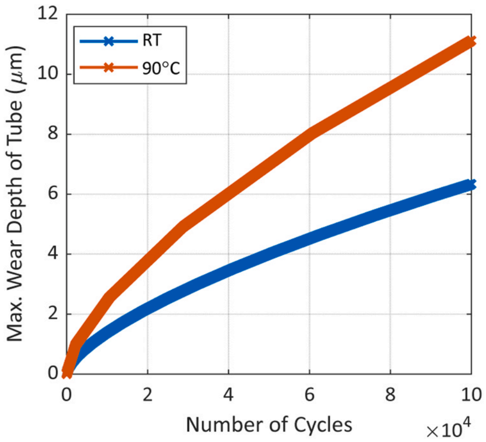

Fig. 28. Maximum wear depth of the tube specimen against the number of cycles for RT and 90 °C.

both cylinders.

4.2. Automotive seat sliding rails

Automotive seat sliding rails consist of a stationary bottom rail, where the top rail can be moved relative to the bottom rail by means of spherical balls or cylindrical rollers. Due to engine vibration, this causes fretting wear between the balls/rollers and the rail [13] reducing the life of the components. Kim and Baek [13] performed ball on flat fretting wear tests to characterize different ball materials against a cold rolled high strength steel (SPFC 440) flat under the gross slip regime.

A simulation of one of the tests using a stainless steel (SUS304) ball was performed, where a schematic of the geometry, loading and material parameters is presented in Fig. 23 and other simulation parameters are summarized in Table 6. The wear coefficient for the flat was based on wear volumes found by Kim and Baek [13] and the wear coefficient for the ball was based on wear volumes found from ball on flat fretting wear tests, where the volumes were averaged for the gross slip cases for SUS304 [60].

The results of the corresponding wear scar of the flat found from Kim and Baek's [13] experiment and from the model are presented in Fig. 24. The model wear depth contour in Fig. 24 (b) shows a wear scar that agrees well in size and shape with the experimental image in Fig. 24 (a). The wear profiles perpendicular to the sliding direction, i.e. the y-direction, are compared in Fig. 24 (c), which show a good agreement in wear scar width and distribution in wear depths, even when using a wear coefficient for the ball from previous testing. The sharp transition at the edges of the model wear scar can be explained by the criterion of contact, where a contact pair will not experience any contact pressure, if it is not in contact. Therefore, if there is no contact pressure for a given contact pair, e.g. just outside the edge of the contact zone, the model will not predict any wear, as this governs the modified Archard's equation. Any other discrepancies between the model and the experiment can be concluded to be the model assuming all debris is ejected during fretting i.e. assuming that only abrasive wear occurs and the model does not consider plastic deformation and adhesive wear causing material transfer due to debris entrapment, showing the limitations of Archard's wear equation. Despite this, the model is able to capture the bulk wear behavior of the flat and capture the negative wear profile. A worn depth contour and worn profile of the ball from the model is also displayed in Fig. 25, where an experimental wear depth was not available in the literature. It can be seen that the maximum wear is located at the center of the scar, as expected, and the magnitude is less than the flat due to the ball having a smaller wear coefficient than the flat. Furthermore, the shape of the wear scar of the ball is circular, while the flat is an ellipse due to the flat being the stationary body.

4.3. Steam generator tubes for nuclear power stations

Steam generators are heat exchangers that are used in the pressurized water reactor of nuclear power stations, which convert heat produced at the reactor core into steam that drives a turbine to generate electricity. These consist of many tubes, which have a flow of contaminated radioactive water and coolant inside, circulated from the reactor core and these act as a barrier for the non-radioactive flow of water. The flow induces vibration, which can cause fretting wear between the contact of the tubes and their supports/anti-vibration bars [7,8]. This leads to failure and therefore, radioactive material can leak into the system, affecting the environment. To understand how to minimize fretting wear for this application, a series of tube on flat tests have been conducted in different environments, temperatures, loading and support materials [7–10]. A simulation of two of these tests performed by Mi et al. [7] were carried out using the fretting wear model, where a schematic of the geometry and loading are shown in Fig. 26. One test was performed at room temperature (RT) and the other at 90 °C, both performed in air under gross slip with all other parameters as presented in Table 7.

To model the contact of the tube, this involved an additional bending compliance, C_b, where the total compliance is given by:

$$C = C_c + C_b \tag{23}$$

where C is the total compliance, C_c is the compliance due to contact described in the contact solver methodology. This was determined using Castigliano's theorem for a curved cantilever beam (by splitting the tube profile into a quarter due to its symmetry) with a point load at the tip, zero rotation at the tip and a reaction contact force along the beam, where the deflections are calculated along different points along the beam, as shown in the Appendix.

Results from the simulations are shown in Fig. 27, which show the worn depth contours of the tube and wear profiles from the two test cases. For both of the worn depth contours in Fig. 27(a) and (b), these show little variation along y-axis with more wear located at the center of the tube profile ($x = 0$ mm), giving a "U" shape worn depth. The maximum wear depth increases by 76% and the wear width increases by 59% from RT to 90 °C, while the corresponding wear coefficients increase by 168%. In Fig. 28, it shows the maximum wear depth of the tube with respect to the number of cycles, which shows a non-linear relationship due to the changing geometry as the material from both bodies wears away. A comparison of the experimental worn profile of the tube with the model is shown in Fig. 27(c) and (d). The experimental worn profile shows an upside down "W", while the model shows a more uniform worn profile. When compared to the experiment, the model shows more of an average, or smooth worn profile. In the experimental studies, the worn depths were reported prior to cleaning the specimen and therefore, the accumulated wear debris could have been present in the worn profiles, which may contribute to some of the variation in the worn profile. In addition, generally there are two types of wear scars for these geometries: "U" shaped and "W" shaped wear scars, where "U" shaped scars are governed by abrasive wear and "W" shaped scars also experiences adhesive wear [61,62]. The modified Archard's wear equation is used for abrasive wear and does not take into account third body behavior. Effective modeling and data of adhesive wear is limited and therefore, further research is needed to incorporate this. Despite this, the model provides a framework for efficient modeling of capturing the bulk wear behavior for aiding the design process, where incorporation of adhesive wear could be added in future work.

5. Conclusions

A numerical modeling methodology has been developed for predicting fretting wear and cylinder on flat geometry cases from previous literature has been used for validation. This study has shown:

- A contact model using the Modified Simplex Method was used in conjunction with the modified Archard wear equation to predict 3D fretting wear scars, wear depths and wear volumes. An interpolation method was also developed for grid refinement to reduce the computational time.
- A combination of linear cycle jumping and an adaptive cycle jumping, based on Taylor series expansion, was applied to the wear calculations and with the grid refinement methodology was able to reduce computational time by 99.9%.
- Simulation times were reduced by 99.9% and 98% when compared with 2D FEA [18] and BEM [30], respectively, despite being a 3D simulation.
- The prediction of fretting wear profiles and pressure distributions followed similar trends and values to previous FEA results [18] and any differences were explained by the inclusion of average cycle pressure in this methodology.
- The maximum wear depth and wear scars of the flat followed an agreement with previous experimental results. Also, wear profiles for a million cycles were compared with previous experimental results, which showed a better agreement for a frequency of 20 Hz compared with higher frequencies due to the model not including debris entrapment and plasticity.
- Three case studies for practical applications were considered: Automotive seat sliding rails, steel wire ropes for industrial applications, and steam generator tubes for nuclear power stations. It was found that the modeled wear scars showed a good agreement in shape, size and depth with the experiment for seat sliding rails and steel wire ropes. However, with the steam generator tubes, there was more variation in the experimental worn profile for the tube in comparison with the model due to the limitation of the modified Archard wear equation not capturing adhesive wear.
- Overall, an efficient fretting wear model was produced that was able to capture the bulk wear behavior of various geometries and loading, which can be used for a design tool to minimize fretting wear damage. Other methods, such as FEA and BEM, showed that simulation times are too long, which become impractical for design.

CRediT authorship contribution statement

Yuen-Ling Kong: Methodology, Investigation, Formal analysis, Data curation, Visualization, Software, Writing – original draft. **Chris J. Bennett:** Conceptualization, Methodology, Writing – review & editing, Supervision, Funding acquisition. **Christopher J Hyde:** Methodology, Writing – review & editing, Supervision.

Declaration of Competing Interest

The authors declare that they have no known competing financial interests or personal relationships that could have appeared to influence the work reported in this paper.

Acknowledgements

The authors would like to acknowledge the Engineering and Physical Science Research Council, UK (Grant EP/P510592/1) and Rolls-Royce plc, UK for providing financial support for this work.

Appendix A

The steam generator tube can be modeled as a curved cantilever beam with a point load at the tip, P, a dummy moment (due to no rotation at the tip due to it being bolted), M_0, and a reaction force, F_j, where j is the nodal number for any position along the beam, as shown in Fig. A1a.

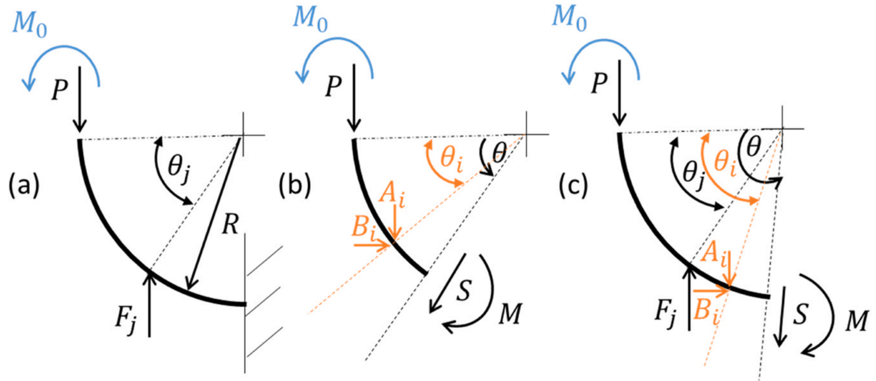

Fig. A1. (a) Schematic of curved cantilever beam and loading, (b) schematics of sections with dummy loads to solve for vertical and horizontal deflections at point i for $\theta_i < \theta_j$ and (c) for $\theta_i > \theta_j$.

Eqs. A1 and A2 show the strain energy for bending and Castigliano's theorem, respectively, which was used to determine the vertical and horizontal deflections (δ_v and δ_h, respectively) at position i using dummy loads in the vertical and horizontal direction (A_i and B_i, respectively).

$$U = \int \frac{M^2}{2EI} R d\theta \tag{A1}$$

$$\phi = \frac{\partial U}{\partial M_0} = 0, \quad \delta_v = \frac{\partial U}{\partial A_i} \quad \textit{and} \quad \delta_h = \frac{\partial U}{\partial B_i} \tag{A2}$$

The dummy moment can be found by using Castigliano's theorem and equating the rotation at the tip to be 0 ($\phi = 0$), which gave the following:

$$M_0 = \frac{2}{\pi}\left[-PR\left(\frac{\pi}{2} - 1\right) + F_j R\left(\left(\frac{\pi}{2} - \theta_j\right)\cos\theta_j - 1 + \sin\theta_j\right)\right] \tag{A3}$$

Once the dummy moment has been found, the deflections at any node i can be found for any load, F_j, at any position j. The solution for $\theta_i < \theta_j$ is given by Eq. A4 (represented in Fig. A1(b)) and for $\theta_i > \theta_j$ is given by Eq. A5 (represented in Fig. A1(c)).

$$\begin{aligned}
\delta_v(\theta_i,\theta_j) = \frac{R^2}{EI}\Bigg[& PR\left(-\frac{1}{2}\sin\left(\frac{\pi}{2}+\theta_i\right) + \left(\frac{\pi}{2}-\theta_i\right)\cos\theta_i - \frac{1}{2}\sin\left(\frac{\pi}{2}-\theta_i\right) + \sin(\theta_i) + \frac{1}{4}\sin(2\theta_i) - \frac{1}{2}(\theta_i) + \frac{\pi}{4} - 1\right) \\
& + M_0\left(\left(\frac{\pi}{2}-\theta_i\right)\cos\theta_i + \sin\theta_i - 1\right) - F_j R\Bigg(-\cos\theta_j\left(\sin\theta_j\cos\left(\frac{\pi}{2}-\theta_j\right) + \cos\theta_i\left(\sin\left(\frac{\pi}{2}-\theta_j\right) - \left(\frac{\pi}{2}-\theta_j\right)\right)\right. \\
& \left. + \cos\theta_j\sin\left(\frac{\pi}{2}-\theta_j\right) - \sin\theta_j\right) + \sin\theta_j\cos\theta_i\left(1 - \cos\left(\frac{\pi}{2}-\theta_j\right)\right) - \frac{1}{4}\sin(2\theta_j) - \frac{1}{2}\theta_j + \frac{\pi}{4}\Bigg)\Bigg]
\end{aligned}$$

$$\begin{aligned}
\delta_h(\theta_i,\theta_j) = \frac{R^2}{EI}\Bigg[& PR\left(\left(\frac{\pi}{2} - \theta_i - 1 + \sin\theta_j\right)\sin\theta_i + \frac{1}{2}\cos(\theta_j+\theta_i) - \frac{1}{2}\cos(\theta_j-\theta_i) - \cos(\theta_i) - \frac{1}{4}\cos(2\theta_i) + \frac{3}{4}\right) \\
& + M_0\left(\left(\frac{\pi}{2}-\theta_i\right)\sin\theta_i - \cos(\theta_i)\right) - F_j R\Bigg(\cos\theta_j\left(\sin\theta_i\left(\frac{\pi}{2} - \theta_j - \sin\left(\frac{\pi}{2}-\theta_j\right)\right) - \sin\theta_j\sin\left(\frac{\pi}{2}-\theta_j\right)\right) \\
& + \sin\theta_j\sin\theta_i\left(1 - \cos\left(\frac{\pi}{2}-\theta_j\right)\right) + \cos^2\theta_j\left(\cos\left(\frac{\pi}{2}-\theta_j\right) - \frac{1}{2}\right)\Bigg)\Bigg]
\end{aligned} \tag{A4}$$

$$\begin{aligned}
\delta_v(\theta_i,\theta_j) = \frac{R^2}{EI}\Bigg[& PR\left(-\frac{1}{2}\sin\left(\frac{\pi}{2}+\theta_i\right) + \left(\frac{\pi}{2}-\theta_i\right)\cos\theta_i - \frac{1}{2}\sin\left(\frac{\pi}{2}-\theta_i\right) + \sin(\theta_i) + \frac{1}{4}\sin(2\theta_i) - \frac{1}{2}(\theta_i) + \frac{\pi}{4} - 1\right) \\
& + M_0\left(\left(\frac{\pi}{2}-\theta_i\right)\cos\theta_i + \sin(\theta_i) - 1\right) - F_j R\Bigg(-\cos\theta_i\left(\sin\theta_i\left(\cos\left(\frac{\pi}{2}-\theta_i\right) - 1\right) + \cos\theta_j\left(\sin\left(\frac{\pi}{2}-\theta_i\right) - \frac{\pi}{2} + \theta_i\right)\right) \\
& - \sin\theta_i\cos\theta_j\left(\cos\left(\frac{\pi}{2}-\theta_i\right) + 1\right) - \frac{1}{4}\sin(2\theta_i) - \cos^2\theta_i\sin\left(\frac{\pi}{2}-\theta_i\right) + \frac{1}{2}\theta_i + \frac{\pi}{4}\Bigg)\Bigg]
\end{aligned}$$

$$\begin{aligned}
\delta_h(\theta_i,\theta_j) = \frac{R^2}{EI}\Bigg[& PR\left(\left(\frac{\pi}{2}-\theta_i\right)\sin\theta_i + \frac{1}{2}\cos\left(\frac{\pi}{2}+\theta_i\right) - \frac{1}{2}\cos\left(\frac{\pi}{2}-\theta_i\right) - \cos\theta_i - \frac{1}{4}\cos(2\theta_i) + \frac{3}{4}\right) + M_0\left(\left(\frac{\pi}{2}-\theta_i\right)\sin\theta_i - \cos(\theta_i)\right) \\
& - F_j R\Bigg(\frac{1}{2}\cos^2\theta_i + \cos\theta_i\left(\cos\theta_j\cos\left(\frac{\pi}{2}-\theta_i\right) - \sin\theta_i\sin\left(\frac{\pi}{2}-\theta_i\right) - \cos\theta_j\right) - \sin\theta_i\left(\sin\theta_i\cos\left(\frac{\pi}{2}-\theta_i\right) + \cos\theta_j\left(\sin\left(\frac{\pi}{2}-\theta_i\right) - \frac{\pi}{2} + \theta_i\right) - \sin\theta_i\right)\Bigg)\Bigg]
\end{aligned} \tag{A5}$$

The resultant of these deflections is used to determine the influence coefficients. It was found for the region of interest around the contact that the influence coefficients vary linearly with F_j, so a unit force can be used to solve these numerically.

References

[1] Zhu MH, Zhou ZR. On the mechanisms of various fretting wear modes. Tribol Int 2011;44:1378–88. https://doi.org/10.1016/j.triboint.2011.02.010.

[2] Curà F, Mura A. Evaluation of the fretting wear damage on crowned splined couplings. Procedia Struct Integr 2017;5:1393–400. https://doi.org/10.1016/j.prostr.2017.07.203.

[3] Ratsimba CHH, McColl IR, Williams EJ, Leen SB, Soh HP. Measurement, analysis and prediction of fretting wear damage in a representative aeroengine spline coupling. Wear 2004;257:1193–206. https://doi.org/10.1016/j.wear.2004.08.003.

[4] Cruzado A, Hartelt M, Wasche R, Urchegui MA, Gomez X. Fretting wear of thin steel wires. Part 1: influence of contact pressure. Wear 2010;268:1409–16. https://doi.org/10.1016/j.wear.2010.02.017.

[5] Lavella M, Botto D. Fretting wear of alloy steels at the blade tip of steam turbines. Wear 2019;426–427:735–40. https://doi.org/10.1016/j.wear.2019.01.039.

[6] Xin L, Yang BB, Wang ZH, Li J, Lu YH, Shoji T. Effect of normal force on fretting wear behavior and mechanism of Alloy 690TT in high temperature water. Wear 2016;368–369:210–8. https://doi.org/10.1016/j.wear.2016.09.018.

[7] Mi X, Wang WX, Xiong XM, Qian H, Tang LC, Xie YC, et al. Investigation of fretting wear behavior of Inconel 690 alloy in tube/plate contact configuration. Wear 2015;328–329:582–90. https://doi.org/10.1016/j.wear.2015.04.003.

[8] Mi X, Cai ZB, Xiong XM, Qian H, Tang LC, Xie YC, et al. Investigation on fretting wear behavior of 690 alloy in water under various temperatures. Tribol Int 2016;100:400–9. https://doi.org/10.1016/j.triboint.2016.05.012.

[9] Guo X, Lai P, Tang L, Lu J, Wang J, Zhang L. Fretting wear of alloy 690 tube mated with different materials in high temperature water. Wear 2018;400–401:119–26. https://doi.org/10.1016/j.wear.2018.01.001.

[10] Lai P, Gao X, Tang L, Guo X, Zhang L. Effect of temperature on fretting wear behavior and mechanism of alloy 690 in water. Nucl Eng Des 2018;327:51–60. https://doi.org/10.1016/j.nucengdes.2017.12.007.

[11] Pompanon F, Laporte J, Fouvry S, Alquier O. Normal force and displacement amplitude influences on silver-plated electrical contacts subjected to fretting wear: a basic friction energy – contact compliance formulation. Wear 2019;426–427:652–61. https://doi.org/10.1016/j.wear.2018.12.010.

[12] Pompanon F, Fouvry S, Alquier O. Influence of humidity on the endurance of silver-plated electrical contacts subjected to fretting wear. Surf Coat Technol 2018;354:246–56. https://doi.org/10.1016/j.surfcoat.2018.07.109.

[13] Kim K, Baek SY. Studies on the influence of a counterpart on fretting wear of cold-rolled high strength steel. Int J Precis Eng Manuf 2018;19:713–9. https://doi.org/10.1007/s12541-018-0085-0.

[14] Dobromirski JM. Variables of fretting process: are there 50 of them? In: Helmi Attia M, Waterhouse RB, editors. Stand. Frett. Fatigue Test Methods Equipment, ASTM STP 1159. Philadelphia: American Society for Testing and Materials; 1992. p. 60–6. https://doi.org/10.1520/stp1159-eb.

[15] Kirk AM, Shipway PH, Sun W, Bennett CJ. The effect of frequency on both the debris and the development of the tribologically transformed structure during fretting wear of a high strength steel. Wear 2019;426–427:694–703. https://doi.org/10.1016/j.wear.2018.12.035.

[16] Fouvry S, Arnaud P, Mignot A, Neubauer P. Contact size, frequency and cyclic normal force effects on Ti–6Al–4V fretting wear processes: an approach combining friction power and contact oxygenation. Tribol Int 2017;113:460–73. https://doi.org/10.1016/j.triboint.2016.12.049.

[17] Xin L, Yang BB, Wang ZH, Li J, Lu YH, Shoji T. Effect of normal force on fretting wear behavior and mechanism of Alloy 690TT in high temperature water. Wear 2016;368–369:210–8. https://doi.org/10.1016/j.wear.2016.09.018.

[18] McColl IR, Ding J, Leen SB. Finite element simulation and experimental validation of fretting wear. Wear 2004;256:1114–27. https://doi.org/10.1016/j.wear.2003.07.001.

[19] Yue T, Wahab MAbdel. Finite element analysis of fretting wear under variable coefficient of friction and different contact regimes. Tribol Int 2017;107:274–82. https://doi.org/10.1016/j.triboint.2016.11.044.

[20] Ding J, Leen SB, Williams EJ, Shipway PH. Finite element simulation of fretting wear-fatigue interaction in spline couplings. Tribol - Mater Surf Interfaces 2008;2:10–24. https://doi.org/10.1179/175158308×320791.

[21] Xue X, Wang S, Li B. Modification methodology of fretting wear in involute spline. Wear 2016;368–369:435–44. https://doi.org/10.1016/j.wear.2016.10.015.

[22] Yue T, Wahab MAbdel. Finite element analysis of stress singularity in partial slip and gross sliding regimes in fretting wear. Wear 2014;321:53–63. https://doi.org/10.1016/j.wear.2014.09.008.

[23] Ding J, McColl IR, Leen SB, Shipway PH. A finite element based approach to simulating the effects of debris on fretting wear. Wear 2007;263:481–91. https://doi.org/10.1016/j.wear.2006.12.056.

[24] J. Ding, S.B. Leen, E.J. Williams, P.H. Shipway, A multi-scale model for fretting wear with oxidation-debris effects, Proc. Inst. Mech. Eng. Part J J. Eng. Tribol. 223 (2009) 1019–1031. https://doi.org/10.1243/13506501JET589.

[25] Zhang L, Ma S, Liu D, Markert B. Fretting wear modelling incorporating cyclic ratcheting deformations and the debris evolution for Ti-6Al-4V. Tribol Int 2019;136:317–31. https://doi.org/10.1002/pamm.201800422.

[26] Mohd Tobi AL, Sun W, Shipway PH. Investigation on the plasticity accumulation of Ti-6Al-4V fretting wear by decoupling the effects of wear and surface profile in finite element modelling. Tribol Int 2017;113:448–59. https://doi.org/10.1016/j.triboint.2016.12.009.

[27] Ding J, Madge J, Leen SB, Williams EJ. Towards the modelling of fretting wear and fatigue interaction in spline couplings. Appl Mech Mater 2006;5–6:165–72. https://doi.org/10.4028/www.scientific.net/AMM.5-6.165.

[28] Cruzado A, Urchegui MA, Gómez X. Finite element modeling and experimental validation of fretting wear scars in thin steel wires. Wear 2012;289:26–38. https://doi.org/10.1016/j.wear.2012.04.018.

[29] Cruzado A, Urchegui MA, Gómez X. Finite element modeling of fretting wear scars in the thin steel wires: application in crossed cylinder arrangements. Wear 2014;318:98–105. https://doi.org/10.1016/j.wear.2014.06.019.

[30] Wan Kim T, Man Moon S, Cho YJ. Prediction of fretting wear using boundary element method. Tribol Int 2011;44:1571–6. https://doi.org/10.1016/j.triboint.2010.10.009.

[31] Rodríguez-Tembleque L, Abascal R, Aliabadi MH. A boundary elements formulation for 3D fretting-wear problems. Eng Anal Bound Elem 2011;35:935–43. https://doi.org/10.1016/j.enganabound.2011.03.002.

[32] Nowell D. Simulation of fretting wear in half-plane geometries—part ii: analysis of the transient wear problem using quadratic programming. J Tribol 2010;132:021402. https://doi.org/10.1115/1.4000733.

[33] Gallego L, Nélias D, Jacq C. A comprehensive method to predict wear and to define the optimum geometry of fretting surfaces. J Tribol 2006;128:476–85. https://doi.org/10.1115/1.2194917.

[34] Gallego L, Nélias D. Modeling of fretting wear under gross slip and partial slip conditions. J Tribol 2007;129:528–35. https://doi.org/10.1115/1.2736436.

[35] Done V, Kesavan D, Krishna M, Chaise T R, Nelias D. Semi analytical fretting wear simulation including wear debris. Tribol Int 2017;109:1–9. https://doi.org/10.1016/j.triboint.2016.12.012.

[36] Gallego L, Nélias D, Deyber S. A fast and efficient contact algorithm for fretting problems applied to fretting modes I, II and III. Wear 2010;268:208–22. https://doi.org/10.1016/j.wear.2009.07.019.

[37] Zhang X, Shen H, Liu J, Deng S, Li X, Cai Z, et al. An efficient numerical model for predicting the torsional fretting wear considering real rough surface. Wear 2015;344–345:32–45. https://doi.org/10.1016/j.wear.2015.10.019.

[38] Gallego L, Fulleringer B, Deyber S, Nélias D. Multiscale computation of fretting wear at the blade/disk interface. Tribol Int 2010;43:708–18. https://doi.org/10.1016/j.triboint.2009.10.011.

[39] Conry TF, Seireg A. A mathematical programming method for design of elastic bodies in contact. J Appl Mech 1971;38:387–92.

[40] Conry TF, Seireg A. A mathematical programming technique for the evaluation of load distribution and optimal modifications for gear systems. J Eng Ind 1973;95:1115–22. https://doi.org/10.1115/1.3438259.

[41] Vijayakar SM, Busby HR, Houser DR. Linearization of multibody frictional contact problems. Comput Struct 1988;29:569–76.

[42] Z. Cao, Y. Shao, M.J. Zuo, X. Liang, Dynamic and quasi-static modeling of planetary gear set considering carrier misalignment error and varying line of action along tooth width, Proc. Inst. Mech. Eng. Part C J. Mech. Eng. Sci. 229 (2015) 1348–1360. https://doi.org/10.1177/0954406214543490.

[43] Hong J, Talbot D, Kahraman A. A semi-analytical load distribution model for side-fit involute splines. Mech Mach Theory 2014;76:39–55. https://doi.org/10.1016/j.mechmachtheory.2014.02.002.

[44] J. Hong, D. Talbot, A. Kahraman, A generalized semi-analytical load distribution model for clearance-fit, major-fit, minor-fit, and mismatched splines, Proc. Inst. Mech. Eng. Part C J. Mech. Eng. Sci. 230 (2016) 1126–1138. https://doi.org/10.1177/0954406215603741.

[45] Li S. Contact problem and numeric method of a planetary drive with small teeth number difference. Mech Mach Theory 2008;43:1065–86. https://doi.org/10.1016/j.mechmachtheory.2007.10.003.

[46] Byung Chae Lee, Byung Man Kwak. A computational method for elasto-plastic contact problems. Comput Struct 1984;18:757–65. https://doi.org/10.1016/0045-7949(84)90022-1.

[47] Johnson KL. Contact mechanics. Cambridge: Cambridge University Press; 1985.

[48] Zhang H, Wang W, Zhang S, Zhao Z. Modeling of finite-length line contact problem with consideration of two free-end surfaces. J Tribol 2016;138. https://doi.org/10.1115/1.4031403.

[49] Stan G, Mays E, Yoo HJ, King SW. The effect of edge compliance on the contact between a spherical indenter and a high-aspect-ratio rectangular fin. Exp Mech 2018;58:1157–67. https://doi.org/10.1007/s11340-018-0421-4.

[50] Love AEH. The stress produced in a semi-infinite solid by pressure on part of the boundary. Philos Trans R Soc A Math Phys Eng Sci 1929;228:377–420. https://doi.org/10.1098/rsta.1929.0009.

[51] Hanson MT, Keer LM. A simplified analysis for an elastic quarter-space. Q J Mech Appl Math 1990;43:561–87. https://doi.org/10.1093/qjmam/43.4.561.

[52] Zhang ZM, Wang W, Wong PL. An explicit solution for the elastic quarter-space problem in matrix formulation. Int J Solids Struct 2013;50:976–80. https://doi.org/10.1016/j.ijsolstr.2012.12.001.

[53] Wang W, Guo L, Wong PL, Zhang ZM. Surface normal deformation in elastic quarter-space. Tribol Int 2017;114:358–64. https://doi.org/10.1016/j.triboint.2017.04.044.

[54] Andersson J, Almqvist A, Larsson R. Numerical simulation of a wear experiment. Wear 2011;271:2947–52. https://doi.org/10.1016/j.wear.2011.06.018.

[55] Nesnas K, Saanouni K. A cycle jumping scheme for numerical integration of coupled damage and viscoplastic models for cyclic loading paths. Rev Eur Des Elem 2000;9:865–91. https://doi.org/10.1080/12506559.2000.10511493.

[56] Labergere C, Saanouni K, Sun ZD, Dhifallah MA, Li Y, Duval JL. Prediction of low cycle fatigue life using cycles jumping integration scheme. Appl Mech Mater 2015;784:308–16. https://doi.org/10.4028/www.scientific.net/amm.784.308.

[57] Ding J, Leen SB, McColl IR. The effect of slip regime on fretting wear-induced stress evolution. Int J Fatigue 2004;26:521–31. https://doi.org/10.1016/j.ijfatigue.2003.09.001.

[58] Hayes EK, Shipway PH. Effect of test conditions on the temperature at which a protective debris bed is formed in fretting of a high strength steel. Wear 2017;376–377:1460–6. https://doi.org/10.1016/j.wear.2017.01.057.

[59] Wang D, Zhang D, Wang S, Ge S. Finite element analysis of hoisting rope and fretting wear evolution and fatigue life estimation of steel wires. Eng Fail Anal 2013;27:173–93. https://doi.org/10.1016/j.engfailanal.2012.08.014.

[60] Kumar SA, Sai SK, Raman SGS, Gnanamoorthy R. Fretting wear behaviour of 304 stainless steel fretted against different counterbody materials. Tribol Mater Surf Interfaces 2013;7:168–74. https://doi.org/10.1179/1751584×13Y.0000000041.

[61] Kirk AM, Sun W, Bennett CJ, Shipway PH. Interaction of displacement amplitude and frequency effects in fretting wear of a high strength steel: impact on debris bed formation and subsurface damage. Wear 2021;482–483:203981. https://doi.org/10.1016/j.wear.2021.203981.

[62] Arnaud P, Baydoun S, Fouvry S. Modeling adhesive and abrasive wear phenomena in fretting interfaces: a multiphysics approach coupling friction energy, third body and contact oxygenation concepts. Tribol Int 2021;161:107077. https://doi.org/10.1016/j.triboint.2021.107077.